

ERT for Northern Infrastructure Protection

Feasibility Study

Alistair Boyle and Andy Adler

Copyright © 2018 A Boyle and A Adler

Andy Adler, Ph.D., P.Eng., Canada Research Professor
Department of Systems and Computer Engineering, Carleton University,
1125 Colonel By Drive, Ottawa, Ontario, K1S 5B6, Canada
Tel: (613) 520-2600 ext. 8785, Fax: (613) 520 5727
Email: adler@sce.carleton.ca

Alistair Boyle, Ph.D., P.Eng., Visiting Researcher
School of Electrical Engineering and Computer Science, University of Ottawa
800 King Edward Avenue, Ottawa, Ontario, K1N 6N5, Canada
Email: aboyle2@uottawa.ca
Post-doctoral Researcher, Research Associate
Department of Systems and Computer Engineering, Carleton University,
1125 Colonel By Drive, Ottawa, Ontario, K1S 5B6, Canada
Email: boyle@sce.carleton.ca Tel: (613) 868-4305

Investigations Jan 2018 to March 2018

Released March 31, 2018, Revision 1.0

Contents

1	Summary	1
1.1	Report organization	1
1.2	Background and Motivation	2
1.3	Technology Details	2
1.4	Objectives	3
1.5	Biography and Research Team	4
2	Background	5
2.1	Electrical Resistance Tomography: overview	5
2.2	Electrical Resistance Tomography – Advantages	8
2.3	To what critical infrastructure can ERT be applied?	9
2.4	What size of changes can be detected in various scenarios?	10
2.5	Electrical Propagation in Materials	10
2.6	Mathematics of electrical current propagation	12
2.7	ERT sensitivity	14

2.8	ERT image reconstruction	15
3	Simulation Models	19
3.1	FEM Meshes	19
3.2	Embankment	24
3.3	Surface	24
3.4	Surface with boreholes	24
4	Results	28
4.1	Sensitivity, Detectability, Drive Strength	28
4.2	Embankment	30
4.3	Surface	30
4.4	Surface with Boreholes	31
5	Discussion	35
5.1	Observations	35
5.2	Limitations and Future work	36
5.3	Conclusions	37
	References	39
	Appendices	42
A	Software	42
A.1	Main Loop	42
A.2	Main Functions	43
A.3	Helper Functions	47
A.4	File Exchange	48

1. Summary

Much critical infrastructure in Canada's north is vulnerable to many different factors, with an especial vulnerability to subsiding ground in areas of thawing permafrost. We have developed technology based on ERT (Electrical Resistance Tomography), which shows promise for low-cost, long term monitoring of changes in permafrost and the associated ground water movement. This report analyses and discusses the feasibility of this approach for detecting state-changes of permafrost and frozen ground from surface and borehole installations.

Overall, our results indicate that detection of the melted liquid in the active layer above permafrost regions is well within the feasibility of ERT monitoring equipment. On the other hand, ERT imaging into the frozen permafrost is much more difficult.

1.1 Report organization

This report is divided into five chapters. In this chapter (chapter 1), we summarize the motivation, results and authors.

In chapter 2, we provide background information on the technology of interest – Electrical Resistivity Tomography – and the technical details of ERT systems. Additionally, we provide background on the geophysical aspects of electrical propagation in the ground, as well as the mathematics of sensitivity and image reconstruction.

In chapter 3, we describe the numerical models which have been developed as part of this report to characterize the scenarios of interest. Numerical models were constructed using finite elements, and adapted to reflect the geometry and electrode positions of the scenarios.

In chapter 4, we describe the results obtained from the numerical models as adapted

to various scenarios of interest. Results are primarily addressed from the point of view of *sensitivity* and *detectability* parameters which we define.

Finally, in chapter 5, we summarize the results of our investigations, discuss the implications, comment on the limitations of the work, and conclude.

1.2 Background and Motivation

There are many pieces of critical infrastructure in Northern Canada that are affected by climate change warming trends [1, 22]. Examples of such critical infrastructure are abundant: municipal (water treatment plants, airports, hospitals), commercial (railways, roadways), and industrial (mine tailings dams, stored toxic waste). Many of these facilities were built under the assumption that existing permafrost zones would remain stable and annual temperature trends would remain unchanged. It is not feasible to rebuild the entirety of this infrastructure which has evolved over the last century, nor is it obvious which infrastructure is most affected, at least until such time as a critical failure occurs.

Of particular interest, critical energy infrastructure such as oil and gas pipelines, electric transmission line towers, and power plants built on frozen ground are subject to the same risk of critical failure due to changing ground conditions. Removal of earth near critical sites, above or below ground, due to excavation (nearby construction or through malicious intent) will also be detectable under certain conditions. Specific pipeline examples are TransCanada's NGTL pipeline (northern Alberta and BC to USA border) the proposed Mackenzie Valley Pipeline (Inuvik, NWT to Alberta), and Enbridge's Line 21 (Norman Wells NWT to Zama, Alberta). The Yukon power and NWT grids are currently isolated from the rest of Canada, though there are plans to build ties into BC, Alberta and Saskatchewan. Most communities of significant size (Dawson, Faro, Whitehorse, Yukon and Yellowknife, Hay River and communities surrounding the Great Slave Lake, NWT) are geographically isolated and rely on safe and consistently available shared power. Other communities (all of Nunavut, many areas of the Yukon and NWT) rely on diesel or natural gas power generation by delivery or from local reserves. Deploying ERT as an all-hazards, remote monitoring tool would allow proactive management of infrastructure risks due to changing ground conditions which would improve system resilience.

1.3 Technology Details

The applicant and his team have developed technology (based on ERT – described below) which shows promise as a relatively inexpensive way to monitor changes in permafrost, soil and groundwater over time. In this proposal, our work analyses the feasibility and potential accuracy of ERT monitoring in permafrost soils.

Electrical Resistivity Tomography (ERT) is a technique which sequentially applies electrical current and takes voltage measurements through electrodes on the surface

(or in boreholes) of the body of interest [2]. The collected measurements are used to reconstruct the resistivity distribution within the earth. In combination with information on topology, these images of ground resistivity can be interpreted as indications of existing ground conditions, providing information on heterogeneous structures and freeze-thaw changes in the near-surface [17, 19]. ERT has the advantage that the instruments are relatively inexpensive, and can operate in a long-distance remote and unattended monitoring capacity for extended periods of time [16, 20].

In related work, we are currently proposing the application of ERT to monitor the safe storage of large quantities of frozen toxic waste (arsenic trioxide) below-ground and for the indefinite future at a former mine site in the north. We are also collaborating with Stephan Gruber, at Carleton University, to characterize permafrost soil conductivity across frequency, soil type, and temperature in a controlled laboratory setting. Previously, ERT has not had significant success in permafrost-soil applications, for two reasons, for which we have developed technical solutions. First, frozen soil is highly resistive at the signal frequencies used in traditional ERT systems; our systems, based on insights from medical imaging applications of the same underlying technology, use higher frequencies. Next, image reconstruction algorithms assume fixed electrode positions and topology, which is not valid for the ground heaves caused by frozen soil [31]. We have developed a new class of algorithms able to detect and compensate for ground movement [10, 11].

1.4 Objectives

The objective of this project is to investigate the feasibility of using ERT for detecting state-changes of permafrost and frozen ground from surface, borehole, and below-ground installations.

Specifically, we focus on answering the following questions:

- As a monitoring technology, what critical infrastructure can ERT be successfully applied to?

We develop criteria by which current and future ERT hardware may be evaluated for application-specific requirements.

- What are the detectability thresholds for various scenarios?

We develop quantitative measures to evaluate the magnitude of dimensional and conductive changes required to render an “unmistakable” change, given particular estimates of measurement noise, geometry, and soil/rock conditions.

The detectability thresholds for changes in frozen ground state are evaluated using simulations with the widely used ERT open source software EIDORS [4, 5], of which we are the primary maintainers. Work is required to develop appropriate models and analyse and generalize results. The report develops parameterized models for surface and underground scenarios, with estimates of expected measurement noise

and an understanding of the detectability of ground state changes under anticipated geophysical conditions.

1.5 Biography and Research Team

The PI, Andy Adler, is a Canada Research Professor in biomedical engineering in Systems and Computer Engineering at Carleton University in Ottawa, Canada. His research interests are broadly in the area of biomedical measurement and robust data analysis. He is author of ten book chapters, four patents, 104 journal and 210 conference papers. Previously, he taught and researched at the University of Ottawa, and worked in senior technology positions at BioDentity (now cryptometrics), AiT (now 3M), DEW Engineering (now ActivCard), and CIL explosives (now Orica). Andy Adler completed a Ph.D. in Biomedical Engineering from the École Polytechnique de Montréal in 1995. He also worked at postdoctoral positions at McGill University and the University of Colorado Health Sciences Center.

Alistair Boyle received a BSc in Electrical Engineering (2002, University of Calgary), an MSc in Biomedical Engineering (2010, Carleton University), and PhD in Electrical and Computer Engineering (2016, Carleton University). His research has focused on geophysical and biomedical applications of impedance tomography; images from direct contact electrical measurements. He worked for 17 years, at Nortel, Seaway Networks, Freescale Semiconductors, and Diablo Technologies designing high speed cryptography, pattern matching, data processing and memory storage into integrated circuits alongside PowerPC and ARM processors, written firmware and application software, and has extensive experience in the electronics labs (PCB design, FPGA design, signal integrity) at gigahertz frequencies. He has taught at Carleton University. Currently, he is a Visiting Researcher in the School of Electrical Engineering and Computer Science at the University of Ottawa and a Post-doctoral Researcher and Research Associate at Carleton University.

The authors represent a team with world class expertise in ERT and permafrost which is directly relevant to monitoring the long-term stability of infrastructure situated at sites on frozen ground. ERT is a potentially very interesting technique which can offer all-hazards long-term and reliable monitoring intelligence. Our team is Canadian and has deep knowledge of ERT technology and its application to both surface and underground geophysics problems around the world.

2. Background

2.1 Electrical Resistance Tomography: overview

Electrical Resistance Tomography (ERT) is a technology to image the electrical properties of the earth using electrical measurements made at electrodes placed on the surface or in boreholes. ERT creates volumetric images of the distribution of resistivity, and, as such is a “tomographic” imaging modality. Electrical measurements are the application of currents or voltages to pairs of electrodes while the voltage across other pairs of electrodes are measured (see figure 2.3).

ERT was invented in 1911 as a means of seeing into the earth and first used to identify iron ore bedding layer boundaries and dip [6]. ERT has subsequently been applied to many other geophysical applications (monitoring of ground water, pollutants, hydrogeology) as well as medical and industrial applications.

An example of an ERT device is shown in figure 2.1. This is the device from ABEM instruments, and it’s size is illustrated by the gloves in the picture. Using this instrument, an “ERT survey” is undertaken, where ground electrodes are placed through wires into the ground. The measurements using the instrument take minutes to hours (depending on the number of electrodes and complexity of the measurement protocol).

Numerous instruments of the type shown in figure 2.1 are available from tens of vendors and cost in the range of several thousand dollars. For the work proposed in this report, this type of instrument is not suitable, because it is designed for specific human-supervised surveys, and not for continuous monitoring.

Instead, we propose to use equipment designed for long-term monitoring, such as the system illustrated in figure 2.2. The illustrated system is part of a project on ERT monitoring of a slow-moving landslide being conducted by the British Geological



Figure 2.1: Example of an ERT instrument, the ABEM TerrameterLS, Image www.ngi.no/upload/48876/TerrameterLS.jpg. The battery provides power at remote sites, and wires connect to installed electrodes.



Figure 2.2: Automated Landslide Electrical Resistivity Tomography (ALERT) system, as part of a research project conducted by the British Geological Survey, located at Hollin Hill, Yorkshire, UK.

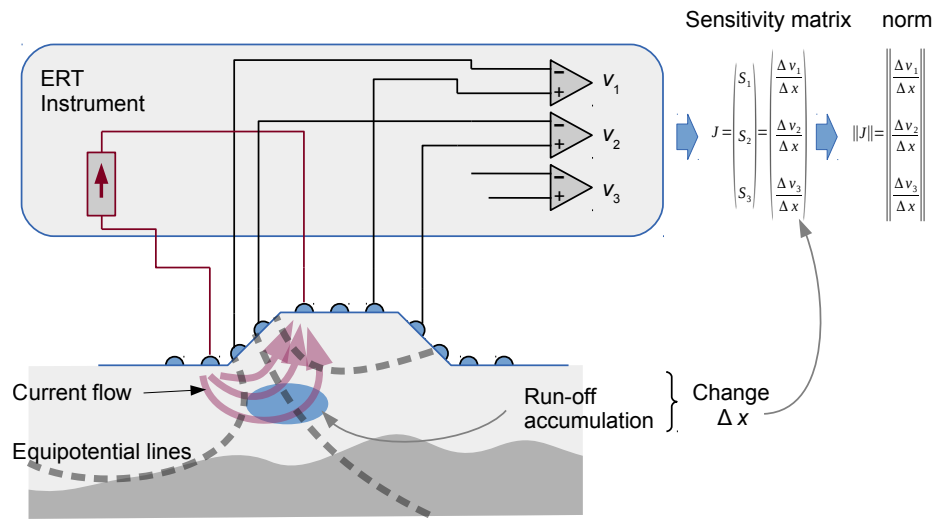


Figure 2.3: Illustration of ERT system and the propagation of current in the ground. Here an embankment is shown. The ERT instrument applies electrical current between a pairs of electrodes and measures voltages, $v_1 \cdots v_n$, at other electrodes. Sensitivity, \mathbf{J} , is ratio between the change in measurements, $\Delta v_1 \cdots \Delta v_n$, from the system for a given change in electrical properties of the ground, Δx . Overall sensitivity is the norm of the sensitivity matrix, $\|\mathbf{J}\|$, as we describe in section 2.7.

Survey. This project has generated continuous ERT data for a section of a hill which is slowly creeping downward. (We were invited to take part in this project because of our expertise in managing ERT data in which electrodes move). There are numerous challenges to continuous geophysical monitoring, from data security, systems robustness, remote (or attended) data upload, power and battery life, as well as from animals and vandalism. We do not address these challenges further in this report, except to note that we are working with several groups who are actively researching how to make such systems robust.

Using the data from ERT, an image is then reconstructed. An example of such images is shown in figure 2.4. Here the resistivity differences across a fault between precambrian schist from tertiary sediments is shown. Pont Péan has been surveyed with ERT for a many decades; it represents a fairly simple geometry and an area of active interest. It was the site of the largest silver mine in Europe for almost 200 years. After 1904 the mine flooded and was abandoned, and is now monitored primarily for reasons of safety[9].

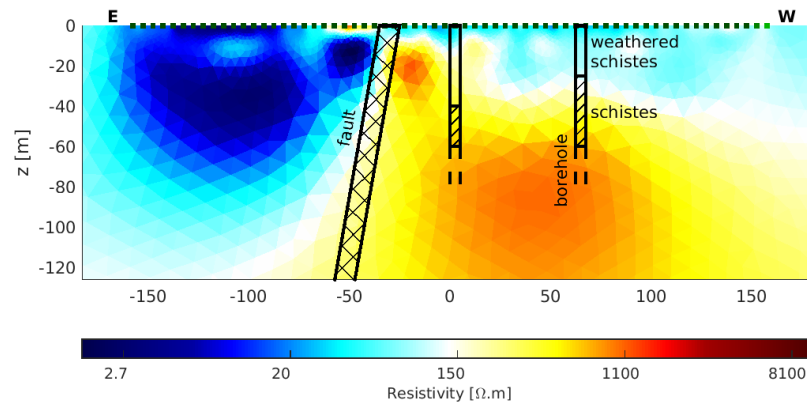


Figure 2.4: Example of an ERT survey, Pont-Péan, France.

2.2 Electrical Resistance Tomography – Advantages

ERT offers many potential advantages for monitoring of critical infrastructure.

- **Potentially inexpensive**

ERT is based on commodity electronics and uses relatively inexpensive low-frequency current sources and analog-to-digital converters. If built in large enough quantities, ERT systems could potentially be in the range of hundreds of dollars. Currently, most systems cost thousands to tens of thousands, but there is a clear downward trend in the price as these systems are built in larger volumes.

- **Reasonably easy/cheap to install**

Installation of an ERT monitoring system requires placement of wires and electrodes into the ground surface. The ability of ERT to “see” into depth means that there is less of a requirement to construct expensive subsurface monitoring installations. Except for the placement of depth electrodes into boreholes, ERT electrode placement is a relatively cheap operation.

- **Sensitive in ground/soil characteristics of interest**

ERT is sensitive to the electrical properties of materials, which offer useful information on the soil characteristics. It is especially sensitive to the concentration of water and its presence on soil pores, such as in clays. From an infrastructure stability point of view, the hydrogeology is often the principle characteristic of interest. ERT’s advantages in soils with larger conductivities contrasts to that abilities of other monitoring technologies such as ground penetrating radar (GPR), which tends to work well in dry soils, but less well in the wetter soils of much of Canada.

- **Sensitive to the ice/water concentrations**

ERT is able to detect the important distinction between frozen and unfrozen concentrations of water in soils, as the electrical conductivity changes dramatically during thawing. This ability of ERT is a useful addition to thermal monitoring,

which is plagued by the problem of latent heat — as frozen ground thaws, a very large energy movement occurs without any change of temperature. This means that thermistor-based monitoring techniques are not able to observe the progression of thawing easily. ERT, on the other hand, offers the advantage of being able to detect the fractional contribution of frozen and unfrozen water concentrations in the ground.

- **Sensitive to temperature variations in the ground**

The conductivity of liquid water increases linearly with temperature, which can be potentially imaged using ERT. This capability is a useful addition to the sensitivity to ice/water concentrations discussed in the previous point.

2.3 To what critical infrastructure can ERT be applied?

In the literature on ERT, and in discussions with experts, we have developed the following list of possible areas of application in terms of critical infrastructure.

- **Road surfaces and critical energy infrastructure**

Critical energy infrastructure such as oil and gas pipelines, electric transmission line towers, and power plants built on frozen ground are subject to risks of critical failure due to changing ground conditions. This infrastructure is generally built on level or nearly level ground and that ground is subject to annual freeze/thaw cycles in the near surface (the active layer), as well as water influx during rainfall and spring run-off. The subsurface may support a layer of permafrost or frozen ground, often within 5 m of the surface. Similarly a layer of high resistivity metamorphic or igneous rock may create a high resistivity layer at a shallow depth in areas where energy infrastructure or roads are constructed.

- **Embankments**

Both rail and roadways are often constructed over embankments which help to isolate the transport surface (rails or pavement) from local geological conditions such as soft soils and unconsolidated rock which may be subject to greater water infiltration and rock/soil movement. Beyond high-traffic transportation routes in Canada, many of these transport corridors constitute critical methods of transporting diesel fuel and goods to “off grid” remote communities, yet are difficult to monitor due to their infrequent use and distance from major centres.

- **Tailing ponds**

Storage of mine waste is an on-going problem for many former mine sites in Canada. The mine waste is stored in tailings ponds which have engineered embankments containing thousands, often millions, of cubic metres of often toxic remnants of ore processing. Tailings ponds are largely located in remote locations, but the embankments require on-going monitoring so that a critical embankment failure, and subsequent release of impounded material, can be avoided. An example of such a spill is the massive 2014 Mount Polley mine

tailings pond spill in BC. Often, remedial measures are relatively inexpensive if the condition is identified prior to a critical failure. Tailing pond embankments are generally straight surfaces, and we lump these simulations in with the road surface investigations, in this work.

2.4 What size of changes can be detected in various scenarios?

Based on the models of critical infrastructure identified in the previous section, there are three important questions we would like to answer:

1. How sensitive is ERT to identifying small changes in conductivity near the electrode array, for example excavations or modifications to the near surface? How far from the electrodes can these changes occur and what magnitude must the resistivity changes be to be identifiable.
2. Can ice or bedrock layers be accurately identified in ERT images and how is the detectability modified under thaw conditions?
3. Does the addition of a small number of borehole electrodes in the near surface improve the overall detectability of the changes of interest?

To understand how these questions can be answered, we provide background on how electricity propagates in the near surface, and how ERT can be used to measure changes in the near surface by reconstructing the most likely resistivity distribution that fits the measurements.

2.5 Electrical Propagation in Materials

The resistivity of materials found in the near surface is highly dependent on microscopic structure, material heterogeneity (mixing), water saturation, temperature, ion concentration and type, and frequency. A complex valued admittivity (conductivity) γ^* can be used to represent the conductivity σ and permittivity ε of a particular material or mixture of materials at a given frequency $\omega = 2\pi f$

$$\frac{1}{\rho^*} = \gamma^* = \sigma + \mathbf{i}\omega\epsilon_0\varepsilon \quad (2.1)$$

with imaginary $\mathbf{i} = \sqrt{-1}$ and the permittivity of free space $\epsilon_0 = 8.8542 \times 10^{-12}$ F/m. Ionic concentration determines water conductivity and freezing/boiling points. Typical water resistivity ranges from 100 Ωm for ultra-pure deionized water, to 0.2 Ωm for typical seawater brines at 25°C. Water conductivity usually varies by +2%/°C near 25°C.

Cole-cole models are often used to model the changes in permittivity over frequency, fitting measured data to multiple “dispersions.” A multiple dispersion Cole–Cole

model [13, 32] for complex-valued permittivity can be constructed as The parameters have been used to calculate a frequency specific complex dielectric constant $\hat{\epsilon}$ as

$$\hat{\epsilon} = \epsilon_{\infty} + \sum_n \frac{\Delta\epsilon_n}{1 + (\mathbf{i}\omega\tau_n)^{(1-\alpha_n)}} + \frac{\sigma_0}{\mathbf{i}\omega\epsilon_0} \quad (2.2)$$

$$\gamma^* = \mathbf{i}\omega\epsilon_0\hat{\epsilon} \quad (2.3)$$

for permittivity ϵ , given the high-frequency permittivity limit ϵ_{∞} , low-frequency conductivity σ_0 , with dispersion time constant τ_n , and $\Delta\epsilon_n = \epsilon_{s,n} - \epsilon_{\infty}$ (the distance of the “static” dielectric constant from the high-frequency limit), and dispersion’s spectral “spread” $0 \leq \alpha_n \leq 1$ over the n dispersion regions. A dispersion spread $\alpha = 0$ is a Debye dispersion model.

Conductivity in sedimentary fluid filled rocks σ is commonly modelled using Archie’s law [7]

$$\sigma = \frac{1}{a} \phi^m S_w^n \sigma_w \quad (2.4)$$

where the water conductivity σ_w , pore volume fraction ϕ , and water saturation S_w along with three empirical constants a , m and n can closely fit measured sedimentary rock conductivities.

A common adaptation of Archie’s law, the Waxman-Smiths equation [33], attempts to account for the effects of clay by adding elements that support variation in ion mobility and concentration

$$\sigma = \frac{1}{a} \phi^m S_w^n \left(\sigma_w + \frac{BQ_v}{S_w} \right) \quad (2.5)$$

where B is the average ion mobility and Q_v is the cation concentration per unit pore volume. These values must typically be fitted to careful lab measurements of core samples to correlate conductivity with saturation [26].

Conduction mechanisms through near surface materials are strongly dependent on frequency (figure 2.5). At low frequency electric current flows through the pore spaces and between grains, while at high frequencies the current is able to flow through the material by taking paths through the pore spaces.

Ice and snow can have very high resistivities when fully frozen. As melting occurs, near the edges of the material, layers of low resistivity water form and ionic conduction within the ice becomes more prevalent.

There is a great deal of work to build good temperature-controlled models of material properties in the low frequency ranges (<1 MHz) common to ERT which we have begun to undertake. For the purposes of this work, we have elected to build a simple resistivity model for our materials: a soil and glacial till with $100 \Omega\text{m}$ resistivity, water with $0.2 \Omega\text{m}$ resistivity and ice (permafrost) or bedrock (for example, basalt or gneiss, as commonly found in the Northwest Territories) in the range of $10^{12} \Omega\text{m}$.

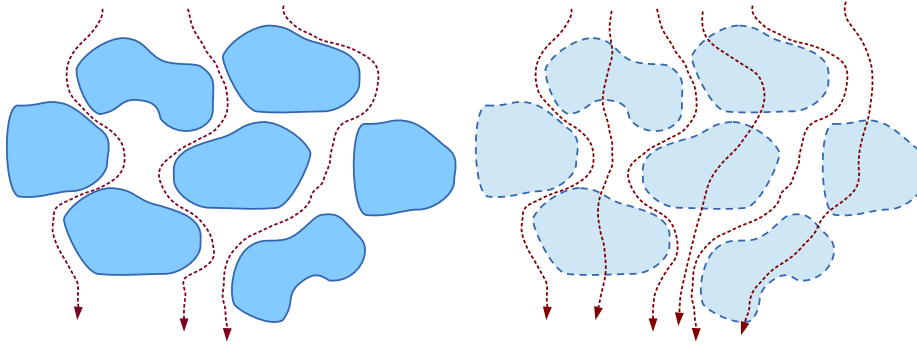


Figure 2.5: Illustration of frequency-sensitive propagation of electricity in porous media. At low frequency (*left*) electrical current flows between grains, while at higher frequency (*right*) electrical current is able to flow through a material’s pore spaces.

2.6 Mathematics of electrical current propagation

The physics of current propagation in the body are determined by Maxwell’s equations. The term “forward problem” has been used to describe the calculation of the current and voltage distribution in the body and then sensitivity of an ERT system as a function of position. To illustrate, figure 2.6 shows current streamlines in a finite element model of the thorax. Current is applied through a pair of electrodes. As the conductivity of the region increases due to the accumulation of conductive run-off during systole, and the pattern of current streamlines and isopotential lines changes. The moving isopotential lines indicate the changes in measures voltage on other body-surface electrodes. The illustrated scenario has very small sensitivity, because the changes are far from the measurement electrodes.

At the relatively low frequencies used in ERT, it can be approximated as an electrostatic system, which is mathematically equivalent to the heat equation. In this limit, electric current propagates diffusively and “spreads out” away from electrodes. This diffusive nature of the physics of low frequency electric current has two main consequences for ERT. First, ERT is extremely sensitive to any changes at or near the electrodes. Reconstructed images can show large artefacts when electrodes move, dry out (changing contact quality) or are incorrectly modelled in terms of shape and size. Next, ERT is much less sensitive further from the electrodes, which is often the region of interest in the interior. The large ratio in sensitivity between the high- and low-sensitivity regions indicates that ERT image reconstruction is “ill conditioned”.

To derive the equations of the ERT forward problem, take a body Ω in three-dimensional space with spatial variable $\vec{x} = (x, y, z)$ outward unit normal \vec{n} . We assume the body isotropic conductivity $\sigma(\vec{x})$, permittivity $\epsilon(\vec{x})$, and permeability $\mu(\vec{x})$, and these properties are potentially inhomogeneous throughout the body.

ERT systems generally apply fixed-frequency currents and voltages to body. For an angular frequency, ω , time-varying properties may be replaced with phasor representations, and the time-derivatives with $\mathbf{j}\omega$. A time-harmonic current density $\vec{J}(\vec{x}, t) = J(\vec{x})e^{-\mathbf{j}\omega t}$ is applied to the surface $\partial\Omega$, and this results, after some settling

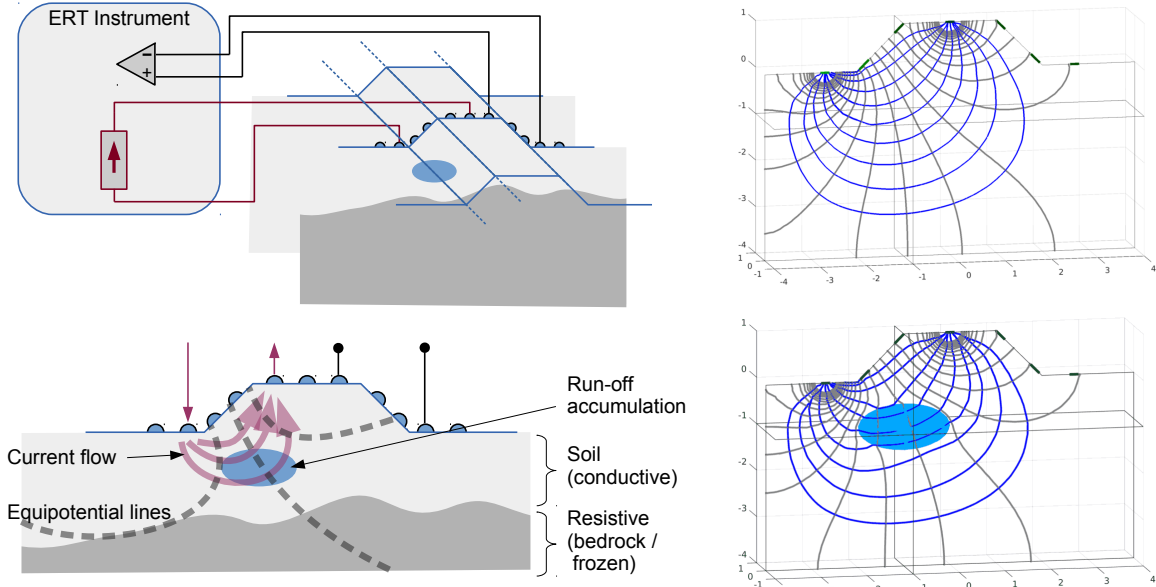


Figure 2.6: Illustration of the propagation of current and the sensitivity of ERT. *Top left:* An ERT instrument is used to make a single measurement at a set of electrodes placed over an embankment; *Bottom left:* Between two current-drive electrodes, a pattern of current flow in the ground is created, and a potential distribution, which can be characterized by equipotential lines. Terrain features such as accumulation of run off or bedrock or permafrost affect the distribution of electrical current; *Top right:* Simulated electrical current flow and equipotential lines for a homogeneous ground, and for (*Bottom right:*) ground with a conductive run-off accumulation region. In each image, a FEM of a volumetric model of the ground is used to simulate the propagation of electric current from a pair of surface electrodes with the indicated current source. Blue lines show current streamlines while the grey lines are isopotential surfaces. Note that fairly large changes in potential near the affected region result in relatively small changes at the electrodes, illustrating the low depth-sensitivity inherent to ERT.

time, in an electric field $\vec{E}(\vec{x}, t) = E(\vec{x})e^{-j\omega t}$ and magnetic field $\vec{H}(\vec{x}, t) = H(\vec{x})e^{-j\omega t}$ in the body. Using Ohm's law, $J = \sigma E$, Maxwell's equations give us,

$$\begin{aligned}\nabla \times E &= j\omega\mu H \\ \nabla \times H &= (\sigma + j\omega\epsilon)E = \sigma^* E\end{aligned}\tag{2.6}$$

We define the complex conductivity or admittivity $\sigma^* = \sigma + j\omega\epsilon$, and use (eqn 2.6) and the identity, $\nabla \cdot (\nabla \times X) = 0$,

$$\nabla \cdot (\nabla \times H) = \nabla \cdot \sigma^* E = 0,\tag{2.7}$$

When permeability and frequency are sufficiently small, we can make the approximation, $\nabla \times E = 0$, in which case the electric field $E = -\nabla\phi$, is uniquely determined by a scalar electric potential, ϕ . This ‘‘quasistatic’’ approximation is valid when the geometric scales of interest are much smaller than the electromagnetic wavelength $(\omega\sqrt{\mu\epsilon})^{-1}$ [21]. For example, in water saturated ground, $\mu \approx 1$ and $\epsilon \leq 80 \times \epsilon_0$, so for $f = 1$ kHz, $(2\pi f\sqrt{\mu\epsilon})^{-1} > 100$ km; the quasistatic approximation is thus valid for the geometries of up to a few hundred meters considered in this report.

These equations define the Laplace (or Poisson's) equation which controls the ERT forward problem

$$\nabla \cdot (\sigma^* \nabla \phi) = 0, \quad (2.8)$$

and is subject to boundary conditions which specify the normal current (Neumann boundary conditions) or potential (Dirichlet boundary conditions) at the electrodes. Additionally, a reference voltage must be specified at some point, either at a ground electrode or elsewhere on the body.

2.7 ERT sensitivity

Calculation of ϕ potential throughout the body requires the solution of (eqn 2.8) for the boundary conditions given by the electrode models and the each of N_C applied pattern of current to the N_E electrodes. No analytic solutions of this equation exist for arbitrary geometries, so it must be instead approximated numerically.

The most common numerical technique is the finite element method (FEM), which is preferred because it allows refinement in regions of high current, such as near the electrodes [15]. In most cases, ERT researchers have used the most simple models, first-order tetrahedral elements. The body is discretized into N_F finite elements, and the complex admittivity in each is represented by a vector $\sigma_F \in \mathbb{C}^{N_F}$. The FEM calculates a voltage distribution throughout the body for each admittivity distribution, σ_F , and applied electrode current distribution, \mathbf{I} .

From the body voltage distribution, a vector of voltages at electrodes is extracted. By successively calculating the electrode voltages for each applied current pattern, a frame, $\mathbf{v} \in \mathbb{C}^{N_m}$, of ERT data is simulated. Many FEM software packages allow vectorized solution of the voltages for multiple current patterns. The maximum number of independent measurements possible on N_E electrodes is $\frac{1}{2}N_E(N_E - 1)$, due to reciprocity (i.e. the sensitivity is unchanged if drive and measurements are interchanged) [24].

The FEM-based forward calculation is represented

$$\mathbf{y} = F(\mathbf{x})|_{\sigma=\sigma_r}. \quad (2.9)$$

For difference ERT, \mathbf{v}_r is calculated at an assumed reference conductivity, σ_r .

For an imaging system, it is important to characterize the sensitivity in terms of the expected change in measured parameters for a given change in parameters of interest. The sensitivity serves to characterize the ability of a given ERT configuration (body shape, electrode positions, stimulation and measurement pattern) to detect contrasts of interest. The sensitivity is also an important part of the image reconstruction process. Sensitivity is represented by a Jacobian, \mathbf{J} , or sensitivity matrix. Each component $[\mathbf{J}]_{i,j}$ represents the sensitivity of measured data, i to image parameter j .

$$\mathbf{J}_{i,j} = \frac{\partial}{\partial \sigma_j} F(\mathbf{x})_i \Big|_{\sigma=\sigma_r}. \quad (2.10)$$

The matrix, \mathbf{J} , may be calculated by direct differentiation of the FEM system matrix formulation [34], and by using adjoint field methods [28]. Direct differentiation requires a custom FEM solver, while the adjoint field methods can accept the output of packaged FEM algorithms, by integrating over the inner product of the electric fields produced by stimulation and measurement patterns in each image element. Efficient implementation of either methods results in the same algorithm [3]. It is sometimes useful to approximate \mathbf{J} using small changes in each image region to calculate a “perturbation Jacobian” [34]. Columns of \mathbf{J} represent the change in measurements, $\partial\mathbf{v}$, due to a conductivity contrast in the corresponding FEM element, while each row represents the relative contribution to each FEM element from the corresponding measurement.

2.8 ERT image reconstruction

Image reconstruction is the term used in the inverse problems and tomographic imaging literature to describe the calculation of an image from projection data. Image reconstruction is typically a challenging problem as it is ill-conditioned and often ill-posed. The ill-conditioning stems from the large difference in sensitivity between regions (the electrodes and the body centre in ERT). ERT is also ill-posed because it is not possible to estimate a large number of image parameters from the limited number of measurements in each data frame.

Image reconstruction is formulated an inverse problem which calculates an estimate, $\hat{\mathbf{x}}$, of the distribution of internal properties, \mathbf{x} , which best explains the measurements, \mathbf{y} . A simplified schema for image reconstruction is shown in figure 2.7, which illustrates the process by which model parameters are iteratively adjusted to fit the measurements (and “prior” image constraints). The reconstructed image is the model after iterations are stopped after convergence.

The most common approach to difference ERT image reconstruction uses a regularized framework to minimize the norm

$$\|\mathbf{y} - F(\hat{\mathbf{x}})\|_{\mathbf{W}}^2 + \lambda^2 \|\hat{\mathbf{x}} - \mathbf{x}_0\|_{\mathbf{Q}}^2, \quad (2.11)$$

where the first term $\mathbf{y} - F(\hat{\mathbf{x}})$ is the “data mismatch” between the measured data and their estimate via the forward model. \mathbf{W} is a data weighting matrix, and represents the inverse covariance of measurements. The second term is the mismatch between the reconstruction estimate, $\hat{\mathbf{x}}$, and an *a priori* estimate of its value, \mathbf{x}_0 . \mathbf{Q} is the “regularization matrix”. The relative weighting between the data and prior mismatch terms is controlled by a hyperparameter, λ . When λ is large, solutions tend to be smooth and more similar to the prior; while, for small λ , solutions have higher spatial resolution, but are noisier and less well conditioned.

The norm (eqn 2.11) may be best understood from a Bayesian maximum a posteriori scheme as follows

$$p(\mathbf{x}|\mathbf{y}) = \frac{p(\mathbf{y}|\mathbf{x})p(\mathbf{x})}{p(\mathbf{y})} \propto p(\mathbf{y}|\mathbf{x})p(\mathbf{x}) \quad (2.12)$$

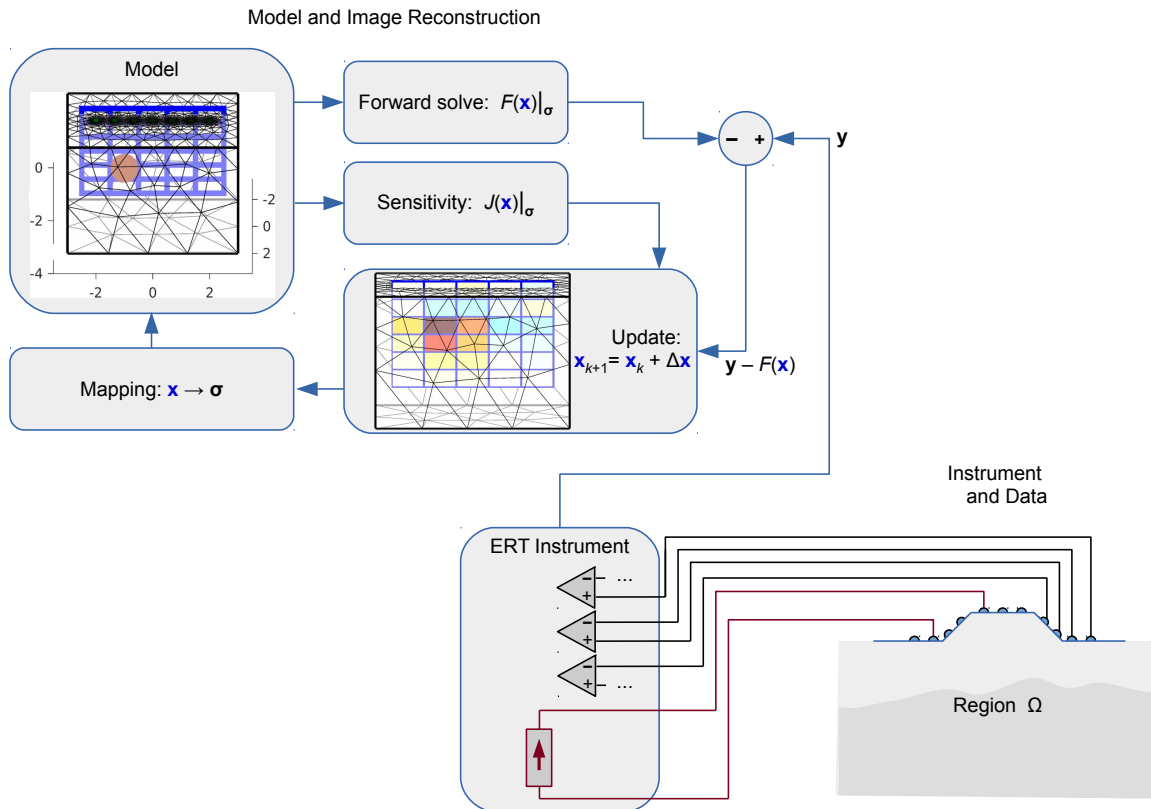


Figure 2.7: Schema for image reconstruction based on model fitting. ERT data, \mathbf{y} , are measured with an instrument from body Ω . Iteratively, a model \mathbf{x}_k is improved by updates, $\Delta \mathbf{x}$, calculated from the mismatch between the current forward estimate and sensitivity, and a prior model. The mapping between image parameters, \mathbf{x} , of a planar slice, and the 3D FEM-based model are illustrated.

where $p(\mathbf{x}|\mathbf{y})$ is the reconstructed quantity of interest, and maybe interpreted as the likelihood of the “correct” image being \mathbf{x} given measured data \mathbf{y} . Here, $p(\mathbf{x})$ is the “a priori” distribution of possible image parameters, and $p(\mathbf{y})$ the distribution of measured data, which is not needed, since the goal is to find the maximum $p(\cdot)$.

The likelihood of measurements \mathbf{y} given image parameters \mathbf{x} is determined by the forward model and the distribution of likely noise from the hardware. Modelling $\mathbf{y} = F(\mathbf{x}) + \nu$, with Gaussian noise $\nu \sim \mathcal{N}(0, \Sigma_n)$, we have

$$p(\mathbf{y}|\mathbf{x}) = \exp\left(-\|\mathbf{y} - F(\mathbf{x})\|_{\Sigma_n^{-1}}^2\right). \quad (2.13)$$

We represent the inverse covariance of the data weighting matrix, as a product, $\Sigma_n^{-1} = \sigma_n^2 \mathbf{W}$, of a scalar noise power, σ_n^2 and a structural matrix \mathbf{W} , which represents the relationship between noise on measurement channels. In most cases, \mathbf{W} is set to be the identity matrix, corresponding to a model of independent and equal measurement channels; however, given a knowledge of the reliability of each measurement channel, \mathbf{W} can be used to represent this reliability during reconstruction [25].

In an inverse problem, it is not sufficient to use only (eqn 2.13) to reconstruct images; the very low sensitivity of measurements to some image parameters (such as voxels far from the boundary) means that small noise values in the data result in large noise in the reconstructed images. Image reconstruction thus requires regularization to impose additional constraints (or penalties) on the images. We review below a number of regularized schemes.

In our opinion, the most natural way to understand regularization is through the Bayesian parameter $p(\mathbf{x})$. This parameter is called the *prior* model, or the *a priori* information, since it describes information about possible images, \mathbf{x} , before any measurements, \mathbf{y} , are made.

Many *prior* models are used; the simplest computationally is a Gaussian distribution $\sim \mathcal{N}(\mathbf{x}_0, \Sigma_x)$, we have

$$p(\mathbf{x}) = \exp\left(-\|\mathbf{x} - \mathbf{x}_0\|_{\Sigma_x^{-1}}^2\right). \quad (2.14)$$

where Σ_x models the expected amplitude and spatial covariance of image parameters. For ERT of changes between two time points, $\mathbf{x}_0 = 0$, since increases and decreases are equally likely. We represent the inverse covariance as a product $\Sigma_x^{-1} = \sigma_x^2 \mathbf{Q}$, of a scalar image power, σ_x^2 and a structural matrix \mathbf{Q} , which is discussed below. The hyperparameter, $\lambda = \frac{\sigma_x}{\sigma_n}$ represents a ratio of the “strength” of the regularization and noise constraints.

From (eqn 2.12), we have

$$\begin{aligned} p(\mathbf{x}|\mathbf{y}) &\propto p(\mathbf{y}|\mathbf{x})p(\mathbf{x}) \\ &= \exp\left(-\|\mathbf{x} - \mathbf{x}_0\|_{\Sigma_x^{-1}}^2\right) \exp\left(-\|\mathbf{y} - F(\mathbf{x})\|_{\Sigma_n^{-1}}^2\right) \\ &\propto \exp\left(-(\|\mathbf{x} - \mathbf{x}_0\|_{\mathbf{W}}^2 + \lambda^2 \|\mathbf{y} - F(\mathbf{x})\|_{\mathbf{Q}}^2)\right). \end{aligned}$$

The MAP (or Maximum a posteriori) solution is the value $\hat{\mathbf{x}}$ which maximizes $p(\mathbf{x}|\mathbf{y})$. It is *a posteriori* in the sense that it is our estimate of the image taking into account (i.e. *after*) the measurements. Thus,

$$\begin{aligned}\hat{\mathbf{x}} &= \underset{\mathbf{x}}{\operatorname{argmax}} e^{-(\|\mathbf{y}-F(\mathbf{x})\|_{\mathbf{W}}^2+\lambda^2\|\mathbf{x}-\mathbf{x}_0\|_{\mathbf{Q}}^2)} \\ &= \underset{\mathbf{x}}{\operatorname{argmin}} \|\mathbf{y}-F(\mathbf{x})\|_{\mathbf{W}}^2+\lambda^2\|\mathbf{x}-\mathbf{x}_0\|_{\mathbf{Q}}^2.\end{aligned}\tag{2.15}$$

The MAP estimate is when the exponential is maximized, and the norm has a minimum.

Starting from an estimate \mathbf{x}_0 , the Gauss-Newton scheme allows an iterative approximation, by, at each step calculating an update $\Delta\mathbf{x}_k$, such that

$$\mathbf{x}_{k+1} = \mathbf{x}_k + \Delta\mathbf{x}_k,\tag{2.16}$$

where at each step, the update would solve the linearized problem, around the current estimate \mathbf{x}_k , using Jacobian, $\mathbf{J}_k = \frac{\partial}{\partial\mathbf{x}}F(\mathbf{x})|_{\mathbf{x}_k}$.

$$\Delta\mathbf{x}_k = \left(\mathbf{J}_k^t\mathbf{W}\mathbf{J}_k + \lambda^2\mathbf{Q}\right)^{-1} \left(\mathbf{J}_k^t\mathbf{W}(\mathbf{y}-F(\mathbf{x}_k)) + \lambda^2\mathbf{Q}(\mathbf{x}_0-\mathbf{x}_k)\right)$$

For an absolute solution, an initial estimate of the solution σ_0 is calculated by fitting a homogeneous (or some low-dimensional) conductivity model to the measurements. Next, in a loop, the same principle operation as difference ERT is computed to find a single-step Gauss-Newton update $\Delta\mathbf{x}_k$, with regularization, measurement covariance, prior, and a Jacobian calculated at the current conductivity estimate. A scaling parameter ($0<\alpha<1$) for this update is determined using a line search and by solving the forward problem at $\mathbf{x}_{k+1} = \mathbf{x}_k + \alpha\Delta\mathbf{x}_k$ then evaluating the data misfit and prior penalty terms to find the minima. This process is repeated until either an iteration limit is exceeded, a tolerance is achieved for the penalty function, or the solution fails to progress. This iterative procedure is illustrated in figure 2.7.

Absolute ERT is more common in geophysics settings where the ability to measure before and after a change can be unusual for many applications. In these geophysics applications, it is also common to parameterize over log conductivity to address the wide range of conductivities that are encountered. Measurements are commonly normalized by dividing the measurements calculated on a forward simulation of the model with a homogeneous 1 S/m conductivity, which are called “apparent resistivity” in geophysics and “measurement normalization” in the biomedical communities. The re-scaling of measurements serves to re-weight the measurement misfit function so that small amplitude measurements will carry equal weight. The measurement re-scaling also impacts estimates of measurement noise which should be similarly scaled, as for example the apparent signal-to-noise ratio should also be rescaled. Scaling conductivity and measurements has a significant effect on appropriate values for regularization parameters which will sometimes change by orders of magnitude.

3. Simulation Models

In order to investigate the feasibility of ERT for monitoring of various infrastructure facilities, we use numerical models to simulate the electrical current propagation, subsurface voltage distribution, and the resulting sensitivities and detectability limits with which changes can be detected. This chapter describes the construction of the simulation models, while the investigation of sensitivity and detectability is considered in chapter 4.

The simulation models are constructed using 2.5D finite element models and are described in detail in the following sections.

3.1 FEM Meshes

Simulations were performed in 2.5D: a 2D finite element method (FEM) mesh (figure 3.1, figure 3.2, figure 3.3) was used to simulate the 3D electric fields around small electrodes using numerical integration of the FEM expansion functions in the additional direction [14]. For the 2.5D method, the resistivity and surface topography are modelled as being uniform in the additional dimension. In our scenarios, we define our axes as: z , the vertical (gravity) direction; x , the transverse (perpendicular to the road or feature) direction; and y , the parallel direction. Thus our 2.5D model is used to assume a uniform distribution in the y direction.

FEM meshes were constructed, representing each surface topology, sub-surface layer, borehole and surface electrode placement: in total nine unique meshes were constructed. The software for mesh definition uses the open source software EIDORS [4] and Netgen [29], which allows for geometry definitions of the model geometry as well as the electrode positions.

The FEM mesh boundaries were extended well beyond the region of interest

Table 3.1: FEM mesh sizes

Model	Subsurface			elements	nodes
	h	p	w		
Rail Embankment	•			7390	3977
		•		6999	3802
			•	10235	5420
Road Surface	•			7448	4030
		•		7054	3833
			•	10300	5456
Road Surface with Borehole	•			8420	4516
		•		7934	4273
			•	10950	5781

Subsurface: h = homogeneous resistivity; p = permafrost layer at 5 m; w = water above permafrost

to account for boundary effects. By constructing images of the current stream lines (figure 2.6), the effect of incorrect boundary conditions was observed and the boundaries were extended until effects on the current stream lines were no longer observed. These boundary effects can also be observed as unexpected increases in the sensitivity far from electrodes. Similarly, the mesh density was increased until unexpected variations in the sensitivity throughout the interior were reduced to low enough levels that the results in the region of interest were stable and appeared “smooth.”

The resulting FEM meshes ranged from 6999 elements (3802 nodes) for the rail embankment model with permafrost, to 10950 elements (5781 nodes) in the road surface and boreholes with a water layer over permafrost model. Meshes for equivalent 3D models were found to be as much as 479 thousand elements, and to take a considerable time to compute the Jacobian required for the following analysis: the use of 2.5D models provides a massive improvement in runtime despite the additional cost of the numerical integrations of multiple Jacobian calculations in the 2.5D method. Mesh sizes are summarized in table 3.1. Meshes are refined at features of higher current density and at locations of changing material properties. Thus, in the meshes illustrated starting at figure 3.1, there is a clear mesh refinement near the surface and the electrodes, as well as at the transition to between the active and permafrost layers.

Simulations were performed using complete electrode models (CEM) [12, 18, 30], and a Wenner stimulation and measurement protocol [8, 23] with a 1 A current between stimulus electrodes. The Wenner stimulation and measurement protocol represents a standard choice for ERT; we do not anticipate significant improvements using adaptive and/or customized protocols for these geometries.

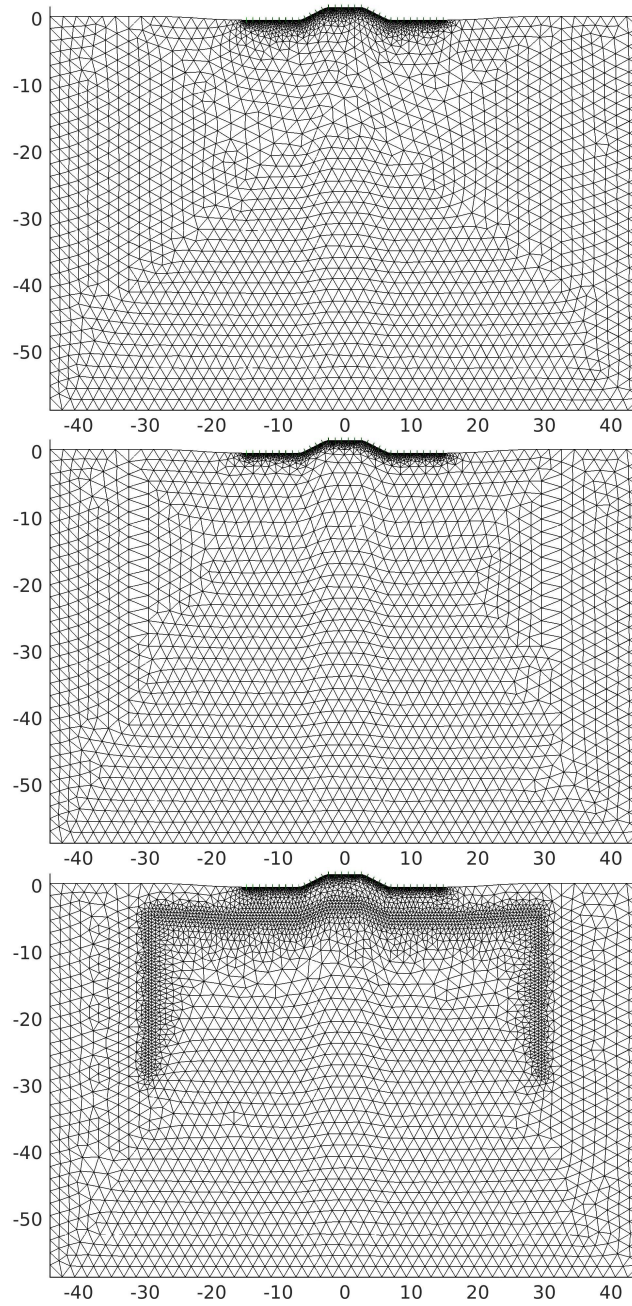


Figure 3.1: FEM meshes used to simulate the low frequency electric fields in 2.5D over a railway embankment; (top) homogeneous model, (middle) a permafrost layer at 5 m depth, (bottom) a thin layer of melt-water over the permafrost

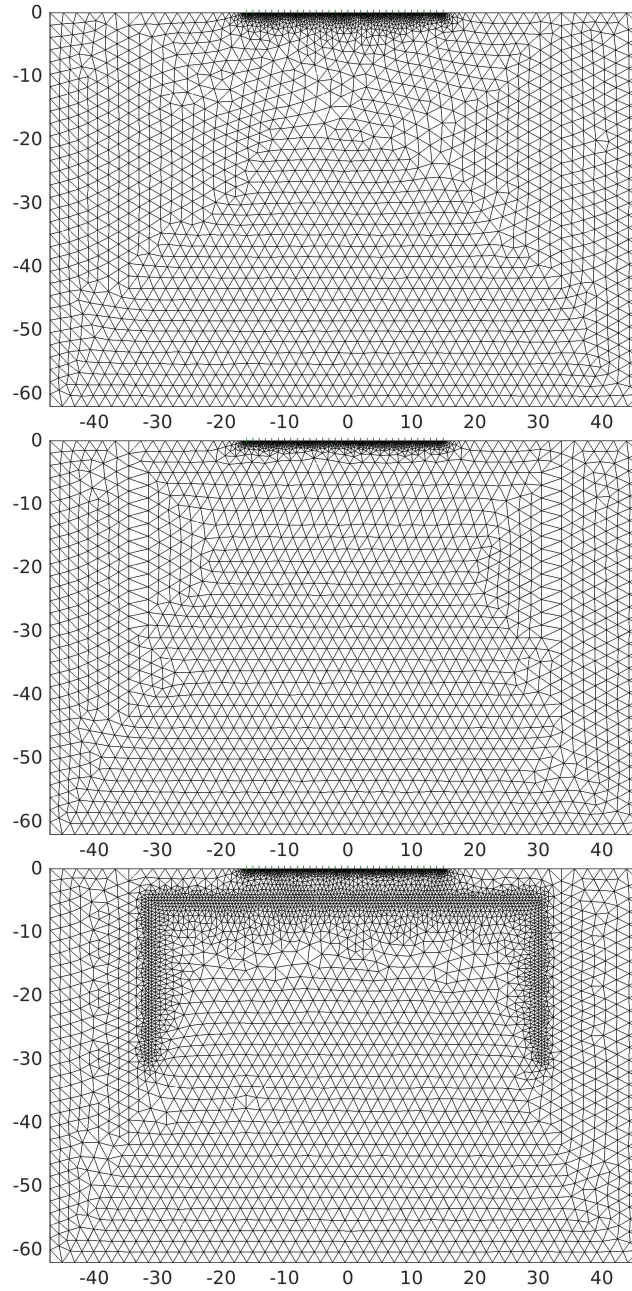


Figure 3.2: FEM meshes used to simulate the low frequency electric fields in 2.5D over a road surface; (top) homogeneous model, (middle) a permafrost layer at 5 m depth, (bottom) a thin layer of melt-water over the permafrost

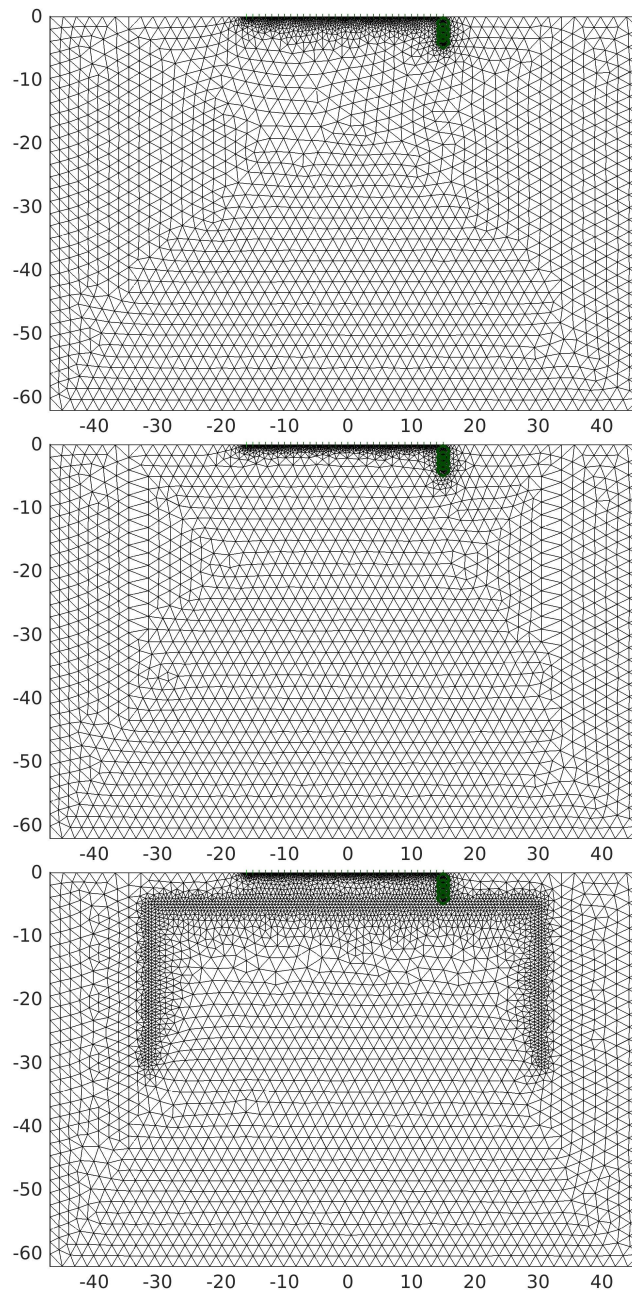


Figure 3.3: FEM meshes used to simulate the low frequency electric fields in 2.5D over a road surface with borehole electrodes at the right end of the electrode array; (top) homogeneous model, (middle) a permafrost layer at 5 m depth, (bottom) a thin layer of melt-water over the permafrost

3.2 Embankment

Railway embankments are built to standards such as the Engineering Guidelines for Private Siding Design and Construction, by Canadian Pacific [27]. A private siding is required to be constructed of a raised embankment consisting of 1.2 m of compacted, clean material, 0.2 m of granular sub-ballast (crushed gravel or stone), and 0.2 m of ballast covering the treated hardwood ties, upon which the rails are nailed. The maximum slope of the embankment is 2:1.

A model of such a private siding embankment is shown in figure 3.4. An array of 32 electrodes in a single line at 1 m spacing have been modelled, running on the surface, under the tracks. An initial simulation using a homogeneous 100 Ωm resistivity ground is presented in this first figure, while subsequent simulations represent the embankment and subsurface according to representative geophysical (electrical) properties for rock, soil, and ice (permafrost) layers.

3.3 Surface

The surface model is similar in most respects to the railway embankment but has a flat (half-space) topology representing an area near a road surface (figure 3.5). Electrodes are spaced at 1 m intervals.

3.4 Surface with boreholes

A model representing a road surface with an adjacent borehole (figure 3.6). The same 32-electrode array is used (section 3.3) with electrodes at 1 m intervals. An additional borehole containing 4 electrodes at 1 m intervals descends from the right-most surface electrode position.

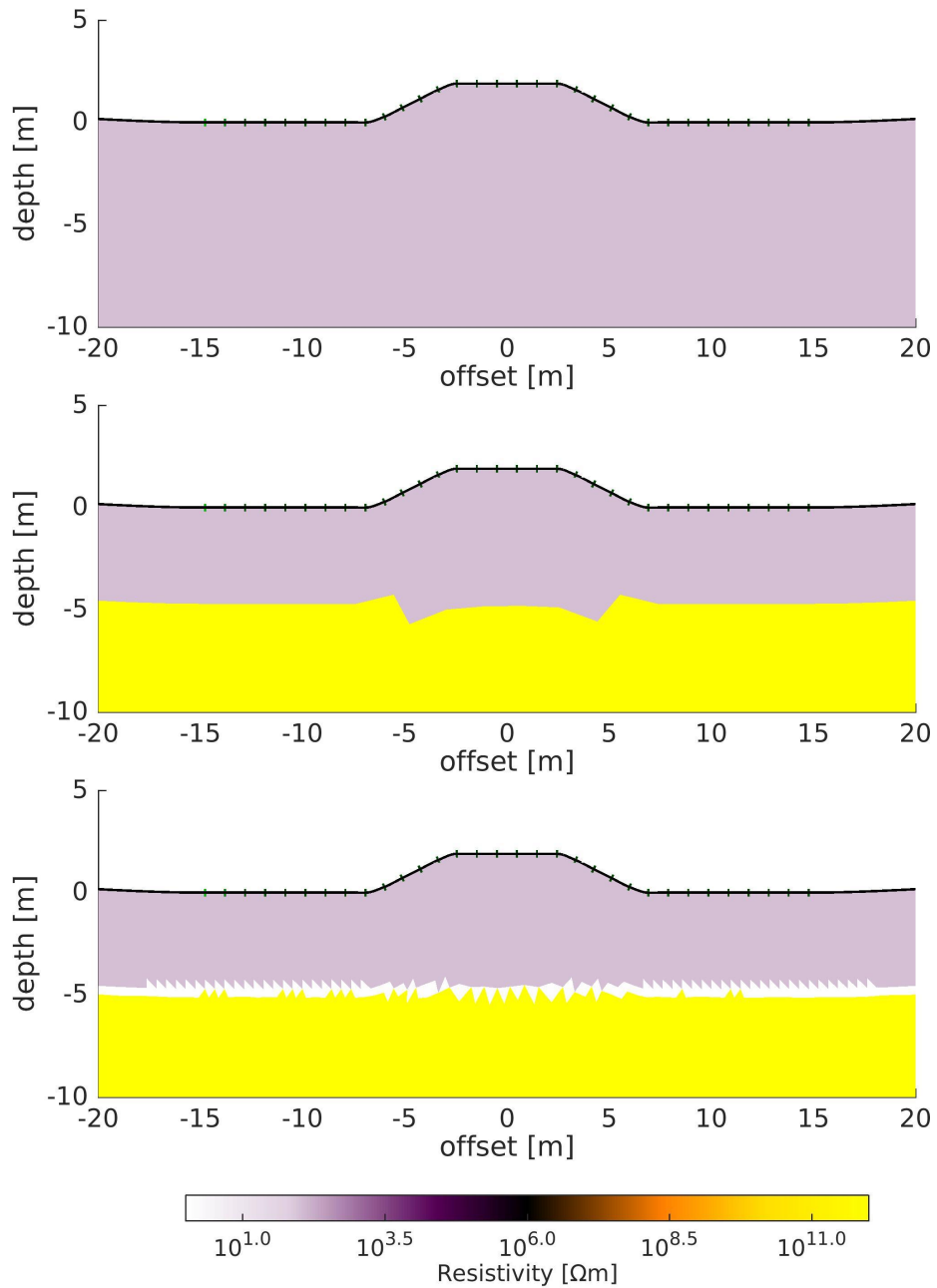


Figure 3.4: Railway embankment in cross-section with a line of 32 electrodes along the surface, under the tracks; (top) homogeneous $100 \Omega\text{m}$ soil, (middle) a $10^{12} \Omega\text{m}$ permafrost layer at 5 m depth, (bottom) a thin layer of $0.2 \Omega\text{m}$ melt-water over the permafrost

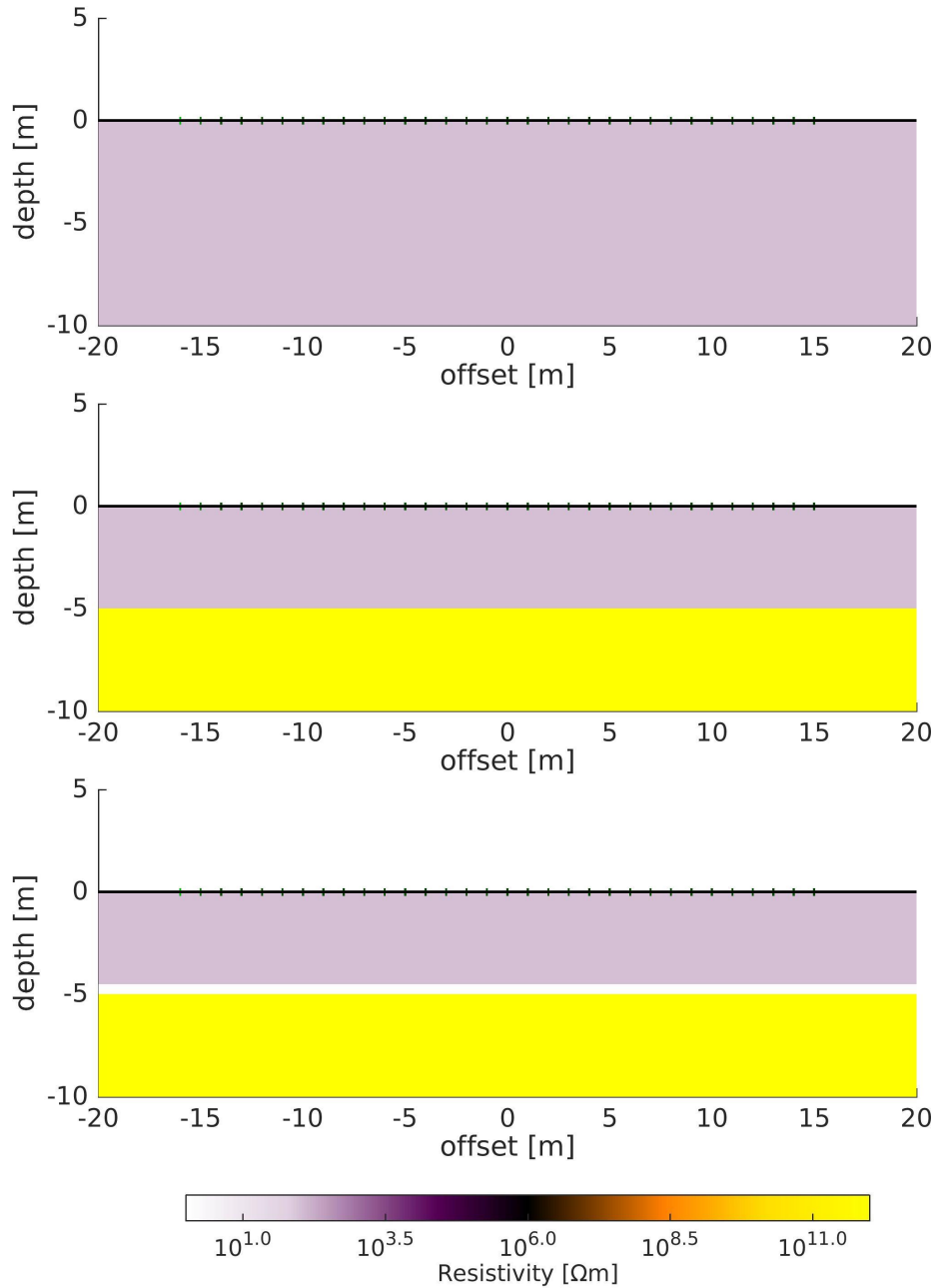


Figure 3.5: A road surface in cross-section with 32 electrodes along the surface; (top) homogeneous $100\ \Omega\text{m}$ soil, (middle) a $10^{12}\ \Omega\text{m}$ permafrost layer at 5 m depth, (bottom) a thin layer of $0.2\ \Omega\text{m}$ melt-water over the permafrost

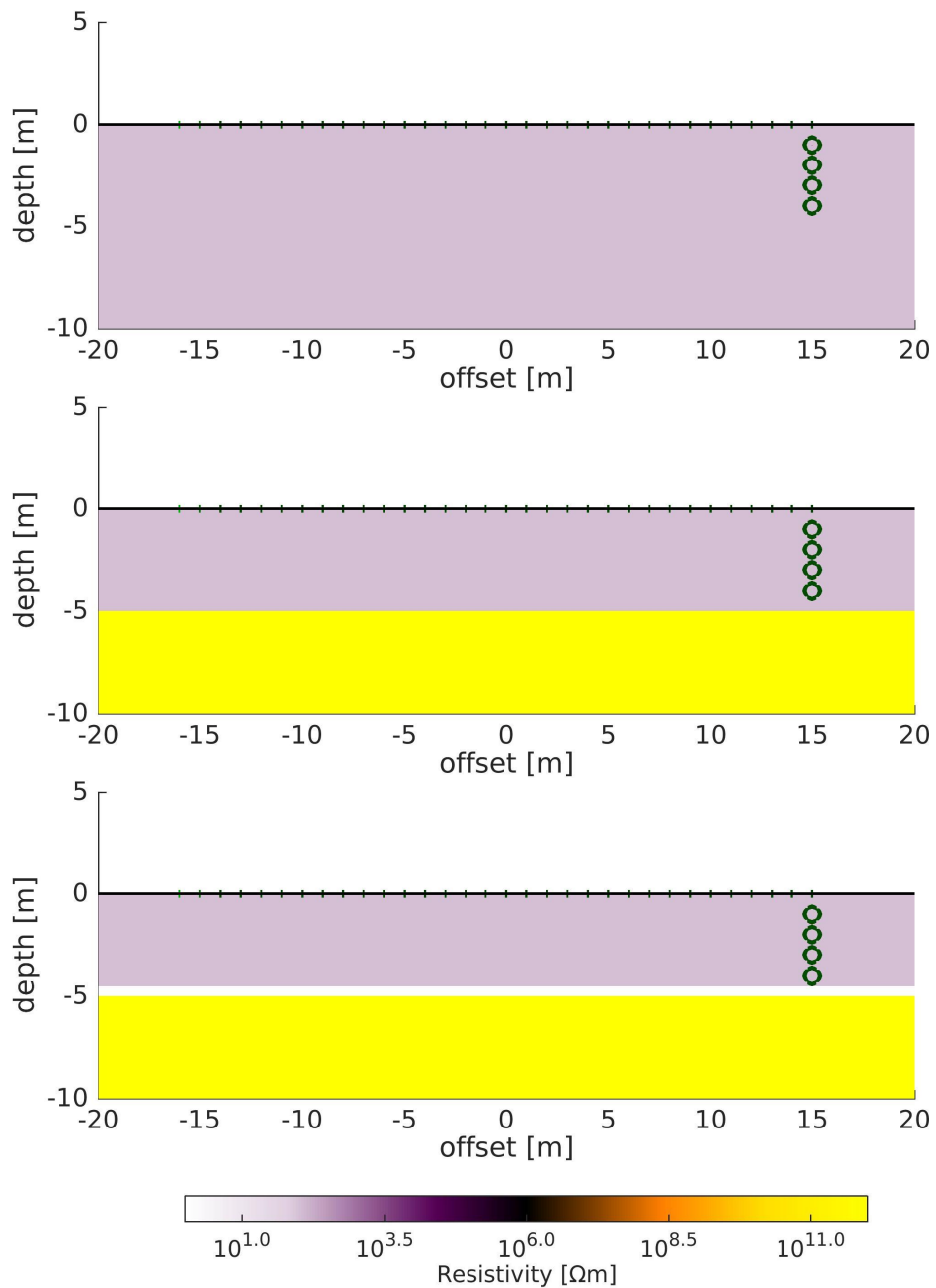


Figure 3.6: A road surface in cross-section with 32 electrodes along the surface (green marks) and a borehole with 4 electrodes at the end of the surface array (green circles); (top) homogeneous $100 \Omega\text{m}$ soil, (middle) a $10^{12} \Omega\text{m}$ permafrost layer at 5 m depth, (bottom) a thin layer of $0.2 \Omega\text{m}$ melt-water over the permafrost

4. Results

4.1 Sensitivity, Detectability, Drive Strength

Using the finite element models developed in chapter 3, we have conducted simulations to determine the sensitivity of ERT as a function of the volumetric distribution of ground properties. From these simulations, the capacity of ERT to detect contrasts of various strengths is determined.

The key parameter which allows determination of the ability of ERT to measure a given change in ground characteristics is the *sensitivity*. For a given sensitivity, the *detectability* is a measure of the reliability with which a given ERT system can “see” a given change. The *drive strength* is the level of electrical stimulation applied. As drive strength increases, measured signal strength increases, which can often improve detectability. Since all systems gave some level of interference or noise, only ERT changes which are larger than these interferences will be detectable. These concepts are illustrated in 4.1, and defined in the subsequent paragraphs.

The *sensitivity* for each element of the FEM mesh is calculated from the matrix-valued Jacobian \mathbf{J} , with rows for each measurement and columns for each mesh element. The Jacobian is often calculated on the conductivity, in which case the chain rule

$$\frac{\partial x}{\partial(1/x)} = \frac{\partial x}{\partial y} = \frac{-1}{y^2} = -x^2 \quad \text{for } y = \frac{1}{x} \quad (4.1)$$

can be used to convert to units of resistivity

$$\mathbf{J}_{\rho,e} = -\sigma_e^2 \mathbf{J}_{\sigma,e} \quad (4.2)$$

for each element (column) e of the Jacobian. The sensitivity of the measurements to a single element perturbation is calculated by taking the column 2-norm of the

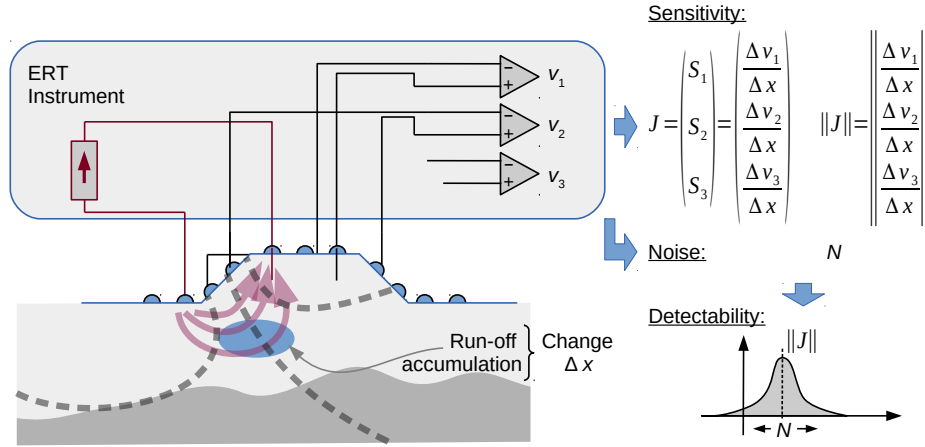


Figure 4.1: Illustration of ERT measurements and the calculation of *sensitivity* and *detectability*. The *drive strength* is controlled by the amplitude of the current source.

Jacobian (Sensitivity matrix)

$$\mathcal{S}_e = \sqrt{\sum_m \mathbf{J}_{m,e}^2} \quad (4.3)$$

for measurements m . This 2-norm is over a single column of the Jacobian for element e and gives a sensitivity in units of $V/\Omega\text{m}$.

The sensitivity is limited by the measurement noise taken as the geometric mean of the individual measurement noise estimates, but limited to some noise floor. For these simulations we have used 1% measurement noise with a noise floor of $1 \mu\text{V}$. The measurement noise \mathcal{N} is then set as

$$\mathcal{N} = \sqrt{\sum_m \left(\frac{v_m}{100} + 10^{-6} \right)^2} \quad (4.4)$$

for the m -th measurement v_m . In these simulations, with Wenner measurements and a 1 A drive strength, the noise floor does not appreciably impact the measurement noise until the noise floor is raised to approximately 1 mV. To look at this another way, if the drive current is reduced we still expect 1% measurement noise, but the $1 \mu\text{V}$ noise floor will not have changed. In other words, the drive strength can be reduced to 1 mA without impacting the noise floor and assuming the measurement noise remains at a 1% level after reducing drive strength. This outcome should not be particularly surprising since the Wenner measurement sequence was selected to give relatively large difference measurements; for a different measurement scheme, near surface resistivity, electrode spacing, and topology the noise performance may differ.

The *detectability* can be found by dividing the sensitivity by the measurement noise to produce an image

$$D_e = \frac{J_e}{\mathcal{N}} \quad (4.5)$$

which indicates a regional, quantitative detectability: regions with detectability greater than unity ($> 1 \Omega^{-1}\text{m}^{-1}$) should be reliably identified for changes in resistivity on the order of $1 \Omega\text{m}$. Interesting resistivity changes in geophysical settings are usually much larger: by scaling the detectability by the expected change in resistivity, one can determine a new threshold for a detectable change from the same image. For example, for a $1 \Omega\text{m}$ to $100 \Omega\text{m}$ ($\times 100$) resistivity change, the region should have a detectability $> 0.01 \Omega^{-1}\text{m}^{-1}$.

4.2 Embankment

Detectability for railway embankments was calculated for a 32-electrode array laid across the embankment (under the tracks) with a 1 m electrode spacing (figure 4.2). Three resistivity models were calculated for the railway embankment with (above) homogeneous soil ($100 \Omega\text{m}$), (middle) an underlying permafrost (ice), basalt, or gneiss at 5 m depth ($10^{12} \Omega\text{m}$), and (bottom) a thin layer of $0.2 \Omega\text{m}$ melt-water over the permafrost.

The homogeneous model ($100 \Omega\text{m}$ resistivity) has detectability which indicates that resistivity changes on the order of $10 \Omega\text{m}$ within an electrode spacing (1 m) of the surface, along the length of the electrode array, are easily detected. Larger changes in resistivity on the order of $100 \Omega\text{m}$, may be detectable out to 5 m below the surface and out to 2.5 m beyond the ends of the electrode array.

The introduction of a layer 5 m below the electrode array of high resistivity, reduces the detectability of changes near the electrode array. On the other hand, changes up to the layer boundary are more detectable. Changes beyond the layer boundary are not very detectable.

If a water layer exists at the interface between the soil and the bedrock or ice, the detectability of changes near the surface resembles that of the case when there is no lower layer of resistive material. Changes up to the boundary are more detectable than in the homogeneous resistivity case. The detectability of resistivity changes is high within the water layer (similar to the regions immediately surrounding electrodes), particularly under the rail embankment.

4.3 Surface

Detectability for an ice road was calculated for a 32-electrode array laid across or alongside the road with a 1 m electrode spacing (figure 4.3). Three resistivity models were calculated for the road with (above) homogeneous soil ($100 \Omega\text{m}$), (middle) an underlying permafrost (ice), basalt, or gneiss at 5 m depth ($10^{12} \Omega\text{m}$), and (bottom) a thin layer of $0.2 \Omega\text{m}$ melt-water over the permafrost.

Similar to the railway embankment, the homogeneous model ($100 \Omega\text{m}$ resistivity) has detectability which indicates that resistivity changes on the order of $10 \Omega\text{m}$ within an electrode spacing (1 m) of the surface, along the length of the electrode array,

are easily detected. Larger changes in resistivity on the order of $100 \Omega\text{m}$, may be detectable out to 5 m below the surface and out to 2.5 m beyond the ends of the electrode array.

As with the railway embankment, the introduction of a layer 5 m below the electrode array of high resistivity, reduces the detectability of changes near the electrode array. On the other hand, changes up to the layer boundary are more detectable. Changes beyond the layer boundary are not very detectable.

If a water layer exists at the interface between the soil and the bedrock or ice, the detectability of changes near the surface resembles that of the case when there is no lower layer of resistive material. Changes up to the boundary are more detectable than in the homogeneous resistivity case. Resistivity changes are highly detectable within the water layer (similar to the regions immediately surrounding electrodes), particularly under the rail embankment. Detectability is not as high as with the railway embankment, where the arrangement of electrodes on the embankment serves to increase detectability below those electrodes.

4.4 Surface with Boreholes

Detectability for a road surface with borehole electrodes at one end of a 32-electrode array was calculated; the borehole contains 4 electrodes in a vertical hole down to a 4 m depth with 1 m spacing (figure 4.4). The same subsurface conditions as section 4.3 were repeated.

Detectability beyond a 1 m radius from the borehole was not significantly different from those observed in section 4.3 for a road surface without boreholes.

From these results it would appear that shallow boreholes do not provide significant advantage, as measured by detectability beyond their immediate vicinity. None the less, placing borehole electrodes near feature interfaces may provide important additional information to constrain reconstruction. For example, in the case of the water layer over permafrost, a depth electrode near the interface would be able to definitively identify when melting conditions occur (as would a thermistor or other contact measurement methods if placed directly on the interface).

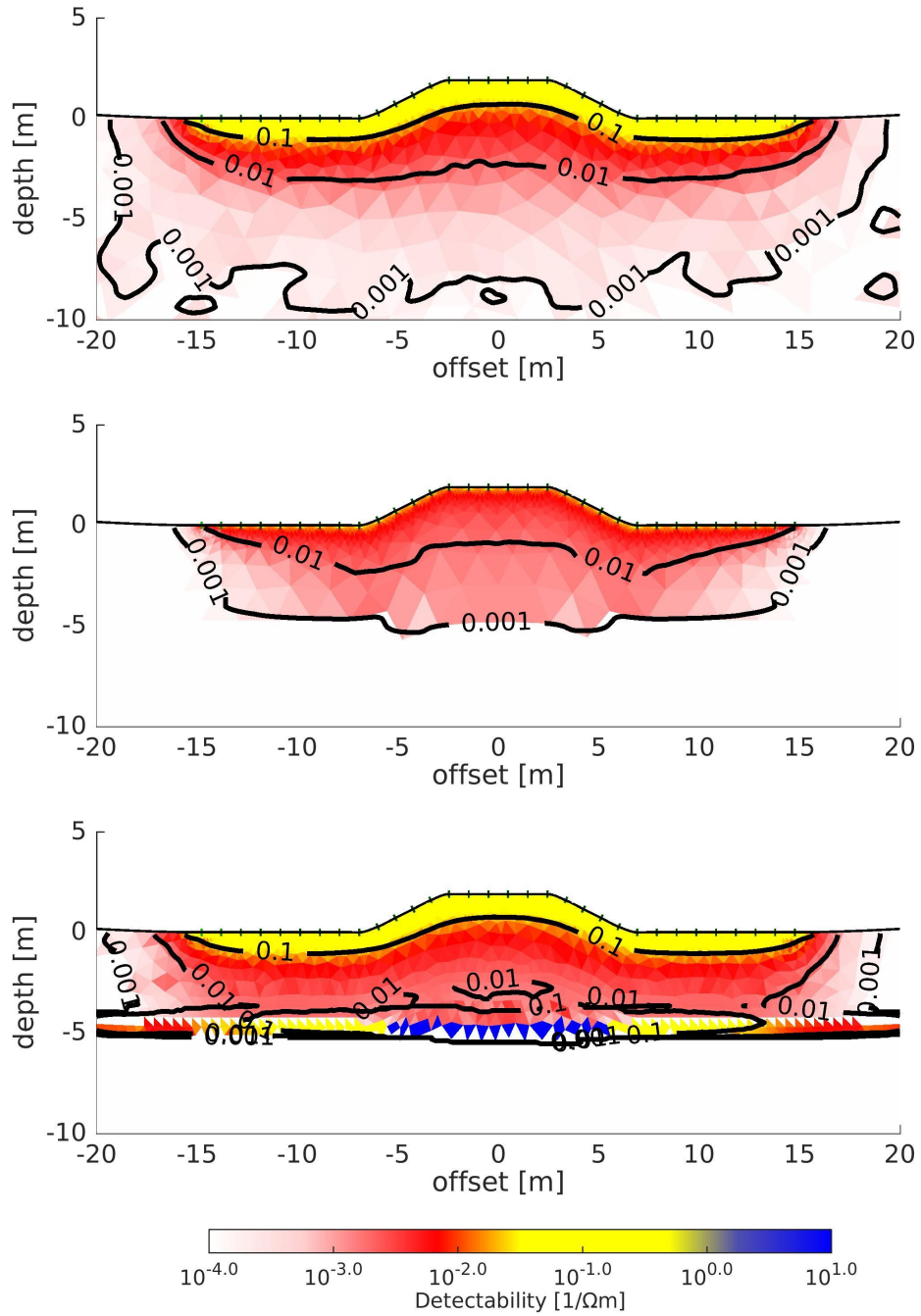


Figure 4.2: Detectability of changes in resistivity under a railway embankment by ERT

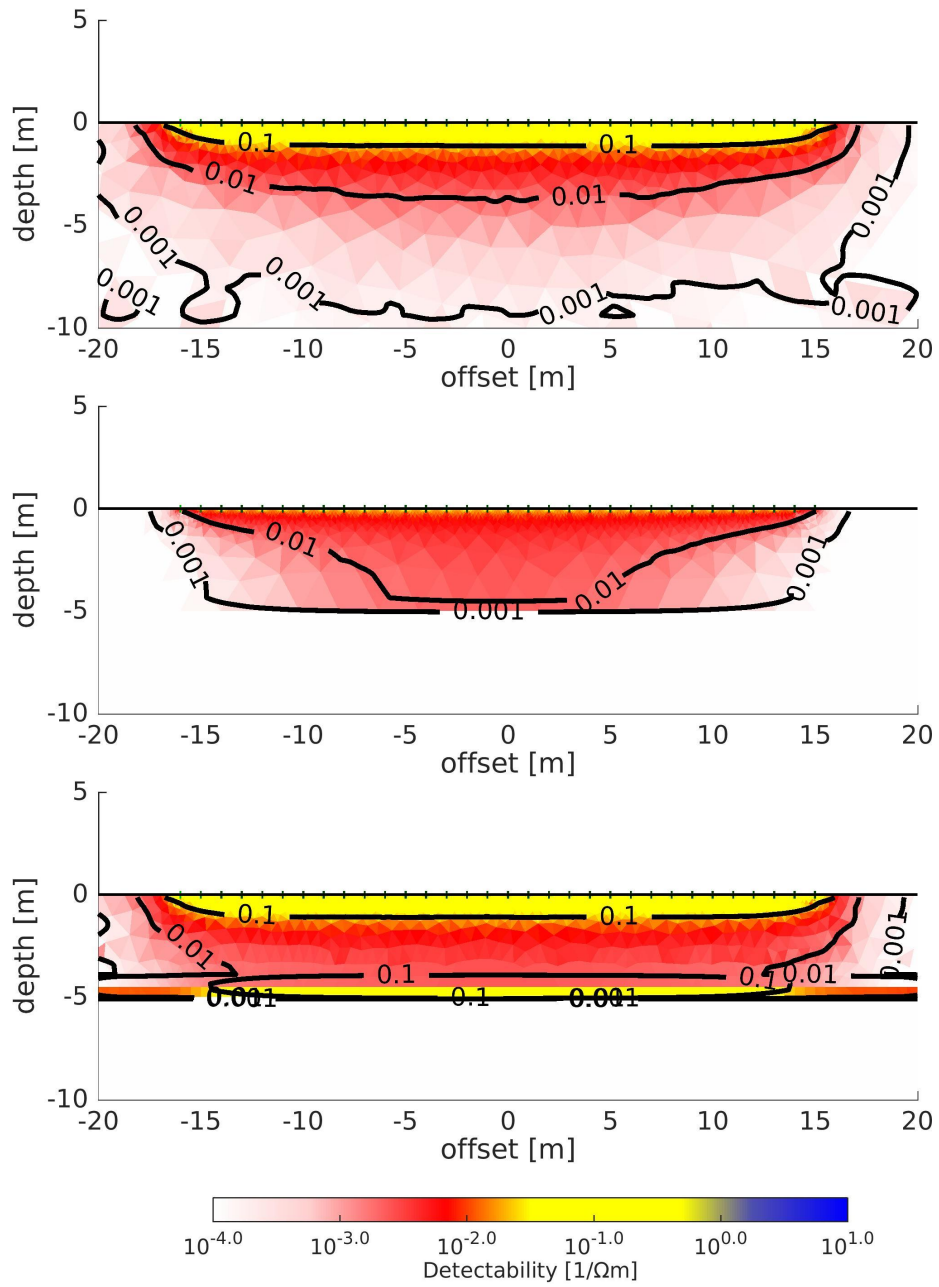


Figure 4.3: Detectability of changes in resistivity under a road surface by ERT

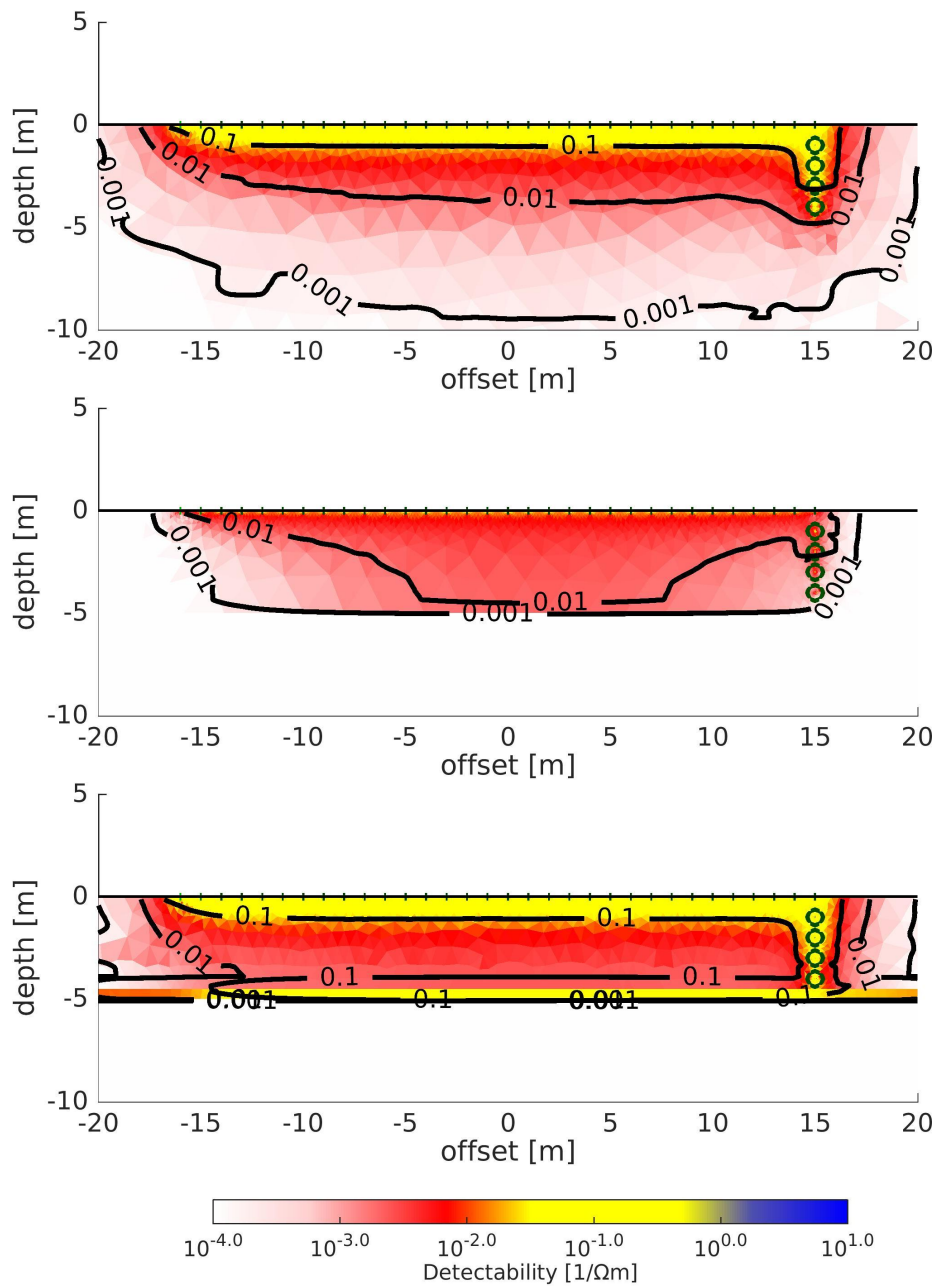


Figure 4.4: Detectability of changes in resistivity under a road surface by ERT, using boreholes

5. Discussion

In this report, we focus on the use of ERT for the monitoring of critical infrastructure. We have developed criteria for the sensitivity and detectability provided by ERT and, based on simulation models (chapter 3), we analyse these parameters for various representative scenarios (chapter 4). Based on our analysis, we develop the following observations.

5.1 Observations

Given the observed regional detectability from simulations in this work, there are four key observations:

1. Changes in resistivity of one order of magnitude ($10\ \Omega\text{m}$) within an electrode spacing (1 m in these simulations) are easily detectable, and changes up to 5 electrode spacings away (5 m with 1 m electrode spacing) are detectable for large resistivity changes on the order of two orders of magnitude ($100\ \Omega\text{m}$). Holes or excavations would result in very large changes in resistivity which might be detectable out to 10 m depth and 5 m beyond the electrode array, based on these detectability plots.
2. Shallow permafrost, frozen ground, or bedrock should be easily detected within 5 electrode spacings (5 m) of the electrode array. In the presence of shallow frozen ground or bedrock, the detectability of small changes near the electrode array is reduced, while detectability in regions near the rock- or ice-soil interface is improved.
3. Melt-water and preferential flow paths near hard boundaries such as ice or bedrock significantly changes the detectable regions by channelling current

flow. Modelling of temperature, ionic concentration, and stored energy of the water content in the near surface may enable accurate long-term monitoring of permafrost/ice changes.

Current equipment commonly used for ERT should be capable of the required sensitivity to monitor these conditions, though re-design for long-term monitoring, rather than single use surveys would be needed. Monitoring of changes within frozen regions or bedrock will require instruments that have considerably higher sensitivity than are generally available, as well as accurate modelling of the near surface conditions above the ice/bedrock.

Shallow boreholes do not appear to improve the detectability of resistivity changes near the surface, within 5 electrode spacings (5 m) of the surface. Borehole electrodes at greater depth (>5 m) may provide useful information that would not be accessible from the surface. Electrodes placed near the interfaces between distinct geological units may provide important information which constrains the reconstruction of wet layers near those boundaries.

5.2 Limitations and Future work

We identify several limitations in the methods used in this report:

- Finite element models represent idealizations of the electrical properties of materials. All sorts of variability occurs which can affect the reliability of the model estimates. For example soils and rocks can have anisotropic properties of variable orientation, as well as strong local variations in temperature, soil/rock type, grain size and fracturing.
- The method of calculating detectability in 2.5D limits the ability, in these simulations, to estimate the detectability of changes adjacent to the electrode array since resistivity changes are assumed to be uniform in the additional dimension.

Simulations in 3D would be able to answer questions about the detectability of changes adjacent to the electrode array, or for electrode configurations where the electrode array is not installed in a line.

- Finite element models with sizes on the order of thousands of nodes were used, primarily driven by the computation-time constraints of this report. For a more high-resolution analysis, these models can be extended to incorporate up to millions of nodes, at the cost of increased computation times.
- We have not taken into account the reconstruction of ERT images in this report, which would be required for use of ERT in these scenarios. Many different approaches to images reconstruction exist which offer various advantages and limitations.

- ERT equipment is currently designed largely for surveys, and few options exist for unattended remote monitoring. For example the equipment shown in figure 2.1, is used by manually identifying the requested settings and performing the scan. We are aware of a few research projects which are developing automated ERT systems designed for continuous monitoring. However, the availability of off-the-shelf equipment for this purpose is still several years away.

5.3 Conclusions

The goal of this report was to focus specifically on the following questions. We summarize our findings:

- As a monitoring technology, what critical infrastructure can ERT be successfully applied to?

In this report, we consider three representative scenarios: an embankment, a horizontal surface, and a surface with boreholes. In each scenario we considered three cases. 1) the scenario above a homogeneous soil; 2) the scenario above homogeneous soil over a 5 m deep highly-resistive layer (gneiss or permafrost); and 3) a scenario like #2, except for a layer of moist soil above the resistive layer, to model ground-water or a melt-water layer above permafrost.

The embankment scenario is designed to represent railway and raised road beds. The horizontal surface can represent many monitoring scenarios, such as for roads and ice roads or for the ground around built up installations. This scenario can also reflect the use of ERT on the surface of containing walls for infrastructure such as tailing ponds.

In high-value infrastructure, the cost of boreholes for a higher resolution and sensitive ERT survey can be justified. Our borehole models can therefore represent cases of built-up infrastructure or for tailing ponds.

- What are the detectability thresholds for various scenarios?

We develop a detectability parameter based on the sensitivity of ERT and the estimated noise and interference in signals from available ERT equipment. Using this parameter, each scenario is simulated using a finite-element model, and results calculated. Images of sensitivity and detectability are shown in figures 3.5, 3.4 and 3.6.

Based on these results, we conclude that ERT shows significant promise as a technology for remote critical infrastructure monitoring. For an electrode spacing of 1 m, large changes in resistivity ($10\ \Omega\text{m}$) are easily detectable up to a depth of 5 m. Shallow permafrost, frozen ground, or bedrock should be easily detected also to a depth of 5 m. Finally, melt-water near a resistive boundary (permafrost or bedrock) creates highly detectable regions. Based on these results, we recommend that ERT be actively researched for its capabilities for continuous remote monitoring of Canada's infrastructure. ERT has numerous advantages (section 2.2) in terms of cost of equipment and installation, which increase the attractiveness of this option.

Bibliography

- [1] G. Oldenborger A. LeBlanc, W. Sladen, and M. Allard. “Infrastructure and climate warming impacts on ground thermal regime, Iqaluit International Airport, southern Baffin Island, Nunavut”. In: *Summary of activities, Canada-Nunavut Geoscience Office (CNGO)* (2014), pages 119–132 (cited on page 2).
- [2] A. Adler and A. Boyle. “Electrical Impedance Tomography: Tissue Properties to Image Measures”. In: *IEEE Transactions on Biomedical Engineering* 64 (11 Nov. 2017), pages 2494–2504. DOI: [10.1109/TBME.2017.2728323](https://doi.org/10.1109/TBME.2017.2728323) (cited on page 3).
- [3] A. Adler, A. Boyle, and W. R. B. Lionheart. “Efficient computations of the Jacobian matrix using different approaches are equivalent”. In: *18th International Conference on Biomedical Applications of Electrical Impedance Tomography*. Dartmouth, USA, June 2017. DOI: [10.5281/zenodo.557093](https://doi.org/10.5281/zenodo.557093) (cited on page 15).
- [4] A. Adler and W. R. B. Lionheart. “Uses and abuses of EIDORS: an extensible software base for EIT”. In: *Physiological Measurement* 27.5 (May 2006), S25–S42 (cited on pages 3, 19, 42).
- [5] A. Adler et al. “EIDORS 3.9”. In: *18th International Conference on Biomedical Applications of Electrical Impedance Tomography*. Dartmouth, USA, June 2017. DOI: [10.5281/zenodo.557093](https://doi.org/10.5281/zenodo.557093) (cited on pages 3, 42).
- [6] L. Allaud and M. Martin. *Schlumberger: The History of a Technique*. John Wiley & Sons, 1977 (cited on page 5).
- [7] G. E. Archie. “The electrical resistivity log as an aid in determining some reservoir characteristics”. In: *Transactions of the American Institute of Mining, Metallurgical, and Petroleum Engineers* 146.1 (1942), pages 54–62 (cited on page 11).
- [8] R. Barker. “Signal contribution sections and their use in resistivity studies”. In: *Geophysical Journal International* 59.1 (Mar. 1979), pages 123–129 (cited on page 20).

- [9] M. Besson. “The Metallogeny of France”. In: *Mining Geology* 32.3 (1982), pages 273–280 (cited on page 7).
- [10] A. Boyle. “Geophysical applications of electrical impedance tomography”. PhD thesis. Ottawa, Canada: Carleton University, 2016 (cited on page 3).
- [11] A. Boyle et al. “Jointly reconstructing ground motion and resistivity for ERT-based slope stability monitoring (in press)”. In: *Geophysical Journal International* (2017). DOI: [10.1093/gji/ggx453](https://doi.org/10.1093/gji/ggx453) (cited on page 3).
- [12] K. S. Cheng et al. “Electrode models for electric current computed tomography”. In: *IEEE Transactions on Biomedical Engineering* 36.9 (Sept. 1989), pages 918–924 (cited on page 20).
- [13] K. S. Cole and R. H. Cole. “Dispersion and absorption in dielectrics. I. alternating current field.” In: *Journal of Chemical Physics* 1 (1941), pages 341–351 (cited on page 11).
- [14] A. Dey and H. Morrison. “Resistivity modelling for arbitrarily shaped two-dimensional structures”. In: *Geophysical Prospecting* 27 (Mar. 1979), pages 106–136 (cited on page 19).
- [15] B Grychtol and A Adler. “FEM electrode refinement for Electrical Impedance Tomography”. In: *Conf. IEEE Eng Med Biol Soc. Okaka, Japan, July 2013*, pages 6429–6432 (cited on page 14).
- [16] C. Hilbich, C. Fuss, and C. Hauck. “Automated time-lapse ERT for improved process analysis and monitoring of frozen ground”. In: *Permafrost and Periglacial Processes* 22.4 (2011), pages 306–319 (cited on page 3).
- [17] C. Hilbich et al. “Monitoring mountain permafrost evolution using electrical resistivity tomography: A 7-year study of seasonal, annual, and long-term variations at Schilthorn, Swiss Alps”. In: *Journal of Geophysical Research: Earth Surface* 113.F1 (2008) (cited on page 3).
- [18] N. Hyvönen. “Complete electrode model of electrical impedance tomography: Approximation properties and characterization of inclusions”. In: *SIAM Journal on Applied Mathematics* 64.3 (Mar. 2004), pages 902–931 (cited on page 20).
- [19] C. Kneisel et al. “Advances in geophysical methods for permafrost investigations”. In: *Permafrost and Periglacial Processes* 19.2 (Apr. 2008), pages 157–178 (cited on page 3).
- [20] O. Kuras et al. “Monitoring hydraulic processes with automated time-lapse electrical resistivity tomography (ALERT)”. In: *Comptes Rendus Geoscience* 341.10-11 (Nov. 2009), pages 868–885 (cited on page 3).
- [21] J Larsen. “Electromagnetics from a quasistatic perspective”. In: *Am J Physics* 75 (2007), pages 230–239 (cited on page 13).
- [22] P. Larsen et al. “Estimating future costs for Alaska public infrastructure at risk from climate change”. In: 18.3 (Aug. 2008), pages 442–457. DOI: [10.1016/j.gloenvcha.2008.03.005](https://doi.org/10.1016/j.gloenvcha.2008.03.005) (cited on page 2).

- [23] M. Loke and R. Barker. “Rapid least-squares inversion of apparent resistivity pseudo-sections by a quasi-Newton method”. In: *Geophysical Prospecting* 44.1 (Jan. 1996), pages 131–152 (cited on page 20).
- [24] HA Lorentz. “The theorem of Poynting concerning the energy in the electromagnetic field and two general propositions concerning the propagation of light”. In: *Amsterdammer Akademie der Wetenschappen* 4 (1896), pages 176–187 (cited on page 14).
- [25] Y Mamatjan et al. “Evaluation and Real-Time Monitoring of Data Quality in Electrical Impedance Tomography”. In: *IEEE T Med Imaging* 32 (2013), pages 1997–2005 (cited on page 17).
- [26] A. Merritt et al. “Measurement and modelling of soil moisture – electrical resistivity relationship for the calibration of time-lapse electrical resistivity tomograms (ERT)”. In: *Journal of Applied Geophysics* (2015). (*in review*) (cited on page 11).
- [27] Canadian Pacific. *Engineering Guidelines for Private Siding Design and Construction*. Technical report. June 2017. URL: <http://www.cpr.ca/en/choose-rail-site/Documents/CP-Engineering-Guidelines-for-Private-Siding-Construction.pdf> (cited on page 24).
- [28] N. Polydorides and W. R. B. Lionheart. “A Matlab toolkit for three-dimensional electrical impedance tomography: a contribution to the Electrical Impedance and Diffuse Optical Reconstruction Software project”. In: *Measurement Science and Technology* 13.12 (2002), pages 1871–1883 (cited on page 15).
- [29] J. Schöberl. “NETGEN An advancing front 2D/3D-mesh generator based on abstract rules”. In: *Computing and visualization in science* 1.1 (1997), pages 41–52 (cited on pages 19, 42).
- [30] E. Somersalo, M. Cheney, and D. Isaacson. “Existence and uniqueness for electrode models for electric current computed tomography”. In: *SIAM Journal on Applied Mathematics* 52.4 (1992), pages 1023–1040 (cited on page 20).
- [31] S. Taber. “The Mechanics of Frost Heaving”. In: *The Journal of Geology* 38.4 (May 1930), pages 303–317 (cited on page 3).
- [32] A. Tarasov and K. Titov. “On the use of the Cole-Cole equations in spectral induced polarization”. In: *Geophysical Journal International* 195.1 (2013), pages 352–356. DOI: [10.1093/gji/ggt251](https://doi.org/10.1093/gji/ggt251) (cited on page 11).
- [33] M. Waxman and L. Smits. “Electrical Conductivities in Oil-Bearing Shaly Sands”. In: *SPE Journal* 8.2 (June 1968), pages 107–122 (cited on page 11).
- [34] T. Yorkey, J. Webster, and W. Tompkins. “Comparing reconstruction algorithms for electrical impedance tomography”. In: *IEEE Transactions on Biomedical Engineering* BME-34.11 (Nov. 1987), pages 843–852 (cited on page 15).

A. Software

Software used for the simulations in this report were completed using EIDORS 3.9+ (SVN revision 5712) [4, 5] using Matlab 2017a. Meshes were generated using NetGen 6.0-beta [29]. The following Matlab scripts were used to generate the figures in this report and can be executed by starting Matlab and initializing EIDORS, then running `nrcan` (Listing A.1).

The `show_fem_log10` code (Listing A.6) makes use of `roundsd` (Listing A.7), which can be found on the Matlab File Exchange: [roundsd.m version 1.6](#) © 2015, François Beauducel, BSD 2-clause license.

A.1 Main Loop

Listing A.1: `nrcan.m`

```
% (C) 2018, A. Boyle
t=tic();
clim_res = [0 12]; % auto
clim_sens = [-4 1]; % auto
5 zoom = [-20 +20 -10 +5];
ne = 32;

for idx = 1:3
    switch idx
10    case 1
        cfg = [inf 100];
    case 2
        cfg = [0 10^2; -5 10^12];
    case 3
15    case 3
        cfg = [0 10^2; -4.5 1/5; -5 10^12];
    otherwise
        error('oops')
```

```

end
for model = {'halfspace', 'railbed', 'borehole'}
20 fprintf('model: %s\n',model{1});
img = nrcan_model(model{1}, ne, cfg);
clf; hh=show_fem(img.fwd_model);
print_img( sprintf('%s%d_fem',model{1},idx), hh, 0);
25 fprintf(' elements: %d\n',size(img.fwd_model.elements,1));
fprintf(' nodes: %d\n',size(img.fwd_model.nodes,1));

fprintf(' - resistivity\n');
[hh,cb]=nrcan_res(img, zoom, clim_res);
print_img( sprintf('%s%d_res',model{1},idx), hh, cb);
30

fprintf(' - sensitivity\n');
[hh,cb]=nrcan_sens(img, zoom, clim_sens);
print_img( sprintf('%s%d_sens',model{1},idx), hh, cb);
end
35 end
toc(t);

```

A.2 Main Functions

Listing A.2: nrcan_model.m

```

function [img, imdl] = nrcan_model(str,ne,z)
% [img, imdl] = nrcan_model(str,ne,Z)
% Models for NRCan report Mar 31, 2018
% str = 'halfspace' halfspace colinear electrode array in 2.5D
5 % 'railbed' electrode array over a rail embankment
% ne = number of electrodes
% Z = layer depths & impedances [ z Ωm ]
% (C) 2018, A. Boyle

10 if nargin < 2
ne = 32;
end
if (nargin < 3) | (length(z) == 0)
z = [inf 1];
15 end
if ~isinf(z(end,1))
z(end+1,:) = [-inf z(1,2)];
end
assert(ne/2 == floor(ne/2), 'ne must be even');
20 assert(all(diff(z(:,1))<0), 'depths must be in descending order');

h2p5 = 'h2p5d';

% layers
25 zs = z(2:end,1)*2/(ne-1); % Z scaled
zs(isinf(zs)) = -2;
nz = length(zs);
tlo = sprintfc('tlo z%d;\n',1:nz-1);
solid = {};
30 for ii = 1:nz-1

```

```

    maxh = abs(diff(zs(ii:ii+1)));
    solid{ii} = sprintf(...
        'solid z%d = orthobrick(-2,%0.6f,%0.6f;2,0,%0.6f) -maxh=%0.6f;\n', ...
        ii, -2*maxh, zs(ii+1), zs(ii), maxh);
35 end
extra_ng_code = [ solid{:}, tlo{:} ];

opt = {};
switch str
40 case 'halfspace'
    line_elec = (linspace(0,ne-1,ne)-ne/2)'*[1 0];
    imdl = mk_geophysics_model(h2p5, line_elec, ...
        {opt{:}, 'extra_ng_code', extra_ng_code });

45 case 'borehole'
    line_elec = (linspace(0,ne-1,ne)-ne/2)'*[1 0];
    % add orthobricks to the model so nodes for
    % boreholes are in the right places
    ne_borehole = 4;
50 zb = -1:-1:-ne_borehole;
    es = 2/(ne-1);
    zb = zb*es; % normalized coordinates
    tlo = sprintfc('tlo bh%d;\n',1:ne_borehole);
    solid = {};
55 for ii = 1:ne_borehole
        solid{ii} = sprintf(...
            'solid bh%d = orthobrick(1,-1,%0.6f;%0.6f,0,%0.6f);\n', ...
            ii, zb(ii)-es/32, +1+es/32, zb(ii));
    end
60 extra_ng_code = [ extra_ng_code solid{:}, tlo{:} ];
    imdl = mk_geophysics_model(h2p5, line_elec, ...
        {opt{:}, 'extra_ng_code', extra_ng_code });
    % add borehole electrodes (PEM)
    borehole = linspace(-1,-ne_borehole,ne_borehole)'*[0 1];
65 fmdl = imdl.fwd_model;
    for ii = 1:length(fmdl.electrode)
        tmp = fmdl.nodes(([fmdl.electrode(ii).nodes]),:);
        x(ii) = (max(tmp(:,1))+min(tmp(:,1)))/2;
    end
70 borehole(:,1) = max(x);
    % assign the extra PEM electrodes at nearest node w/o a stim pattern
    for ii = 1:size(borehole,1)
        [~,idx] = min(sum(bsxfun(@minus, fmdl.nodes, borehole(ii,:)).^2,2).^0.5);
        imdl.fwd_model.electrode(end+1) = imdl.fwd_model.electrode(1);
75 imdl.fwd_model.electrode(end).nodes = idx;
    end
    % rebuild stim/meas sequence
    imdl.fwd_model.stimulation = stim_pattern_geophys(ne+ne_borehole, 'Wenner');

80 case 'railbed'
    % see Canadian Pacific,
    % Engineering Guidelines for Private Siding Design and Construction,
    % June 2017
    embankment = [5.5/2 1.5+0.4; 5.5/2+(1.5+0.4)*2 0; 30 0]';
85 embankment = [ fliplr(embankment) embankment ];
    embankment(1,1:end/2) = -embankment(1,1:end/2);

```

```

    X = embankment(1,:); Y = embankment(2,:);
    Xm = min(X); X = X - Xm; Ym = min(Y); Y = Y - Ym;
    D = cumsum([ 0 sqrt(diff(X).^2+diff(Y).^2) ]);
90  Dq = linspace( max(D)*1/4, max(D)*3/4, ne );
    Xq = interp1(D,X,Dq);
    Yq = interp1(X,Y,Xq) + Ym;
    Xq = Xq + Xm;
    rail_elec = [Xq; Yq]';
95  imdl = mk_geophysics_model(h2p5, rail_elec, ...
        {opt{:}, 'extra_ng_code', extra_ng_code });
    otherwise
        error('oops');
    end
100  imdl.name = str;

    img = mk_image(imdl,1);
    img.name = imdl.name;
105  img.elem_data(:) = 1/z(1,2);
    fprintf( '%s\n  background: 10^%+0.1f Ωm\n', ...
        str, -log10(img.elem_data(1)) );
    nn = img.fwd_model.elems;
    ctrs = interp_mesh(img.fwd_model); Zimg = ctrs(:,2);
110  for idx = 2:nz
        ee = find((Zimg < z(idx,1)) & (Zimg > z(idx+1,1)));
        img.elem_data(ee) = 1/z(idx,2);
        assert(length(ee)>0,sprintf('didn''t find layer%d',idx-1));
115  fprintf( '  layer %2d (%+0.1fm): 10^%+0.1f Ωm (%d elements)\n', ...
            idx-1, z(idx,1), -log10(img.elem_data(ee(1))), length(ee) );
    end
end

```

Listing A.3: nrcan_res.m

```

function [hh,cb]=nrcan_sens(img, zoom, clim)
% (C) 2018, A. Boyle
    if nargin < 2
        zoom = []; % auto
5    end
    if nargin < 3
        clim = []; % auto
    end

10  img.calc_colours.cmap_type = 'ice';
    img.elem_data = 1./img.elem_data;
    if length(unique(img.elem_data)) == 1
        img.elem_data(1) = img.elem_data(1)*10;
        img.elem_data(2) = img.elem_data(2)*100;
15  end

    cb_title = 'Resistivity [Ωm]';
    [hh, cb] = show_fem_log10(img, zoom, clim, cb_title);

```

Listing A.4: nrcan_sens.m

```

function [hh,cb]=nrcan_sens(img, zoom, clim)
% (C) 2018, A. Boyle
    if nargin < 2
        zoom = []; % auto
5    end
    if nargin < 3
        clim = []; % auto
    end

10    J = calc_jacobian(img);
    S = - spdiag(img.elem_data.^2); % scaling for J [ $V/\Omega m$ ]
    JS = J*S;
    vol = get_elem_volume(img.fwd_model);

15    n_per = 0.01; % noise, in percent: 1%
    n_min = 1e-6; % noise floor: 1nV for 1A
    vi = fwd_solve(img); vi = vi.meas;
    vi = (abs(vi) * n_per) + n_min;

20    % normalize measurements:  $V/I = R$  (Ohms)
    nn = 1;
    stim = img.fwd_model.stimulation;
    for ii = 1:length(stim)
        assert(size(stim(ii).stim_pattern,2)==1);
25        for jj = 1:size(stim(ii).meas_pattern,1)
            I = max(stim(ii).stim_pattern(:,1)) * max(stim(ii).meas_pattern(jj,:));
            JS(nn,:) = JS(nn,:) / I;
            vi(nn) = vi(nn) / I;
            nn = nn +1;
30        end
    end
    fprintf('  noise: %e  $\Omega n$ ', norm(vi));

    img.elem_data = sqrt(sum(JS.^2,1)./(vol.^2)) / norm(vi);
35    img.calc_colours.cmap_type = 'flame';

    %cb_title = 'Sensitivity [ $\Omega/\Omega m$ ]';
    cb_title = 'Detectability [ $1/\Omega m$ ]';
    [hh, cb] = show_fem_log10(img, zoom, clim, cb_title);

40    % add contours to plot
    hold on
    x = linspace(-20,+20,200);
    y = linspace(-10,5,200);
45    img.fwd_model.mdl_slice_mapper.x_pts = x;
    img.fwd_model.mdl_slice_mapper.y_pts = y;
    map = mdl_slice_mapper(img.fwd_model, 'elem');
    v = map*nan;
    v(map>0) = img.elem_data(map(map>0));
50    w=round(length(find(x>0 & x<0.5))/2)*2;
    h=round(length(find(y>0 & y<0.5))/2)*2;
    v = conv2(v,ones(h+w)/(h*w)); % smooth contours
    vt = v(w/2+1:size(map,1)+w/2, ...
           h/2+1:size(map,2)+h/2);
55    vv = [0.1 0.01, 0.001];
    [~, cc] = contour(x,y,vt,vv, 'ShowText', 'on', 'LineWidth', 2, 'LineColor', 'black');

```

```
hh = [hh cc];
hold off;
```

A.3 Helper Functions

Listing A.5: print_img.m

```
function print_img(str, hh, cb)
% print_img(str, hh, cb)
% str - filename prefix, hh - img handles, cb - colorbar handle
print([ str '.jpg'], '-djpeg', '-r400'); % img + colorbar
5 if cb ~= 0
    set(cb, 'Visible', 'off');
    print([ str '-img.jpg'], '-djpeg', '-r400'); % img only
    set(cb, 'Visible', 'on');
    set(hh, 'Visible', 'off');
10 print([ str '-cb.jpg'], '-djpeg', '-r400'); % colorbar only
    set(hh, 'Visible', 'on');
end
```

Listing A.6: show_fem_log10.m

```
function [hh,cb]=show_fem_log10(img, zoom, clim, cb_title)
img.elem_data = log10(img.elem_data);

if length(clim) == 0
5   clim = [min(img.elem_data)/2 max(img.elem_data)];
   if diff(clim) < 2
       clim = mean(clim);
       clim = [clim- 1, clim+1];
   end
10 end
img.calc_colours.ref_level = sum(clim)/2;
img.calc_colours.clim = diff(clim)/2;
clf; hh=show_fem(img,1);
ylabel('depth [m]'); xlabel('offset [m]');

15
cb=eidors_colourbar(img);
t=get(cb, 'YTickLabel');
set(cb, 'Location', 'SouthOutside');
set(cb, 'XTickLabel', sprintfc('10^{%0.1f}', log10(roundsd(10.^(str2num(t)), 2))));
20 % 'Resistivity': units = 'Ωm';
% 'Conductivity': units = 'S/m';
% 'Sensitivity Ratio': units = '';
% 'Sensitivity' (percent): units = '%';
% 'Sensitivity' (voltage measurements, resistivity): units = 'VΩ-1m-1';
25 % 'Sensitivity' (voltage measurements, conductivity): units = 'VS-1m';
% 'Sensitivity' (normalized measurements, conductivity): units = 'ΩS-1m';
cb.Label.String = [ cb_title ];
p=cb.Position;
p(2)=p(2)-p(4)/2;
30 p(4)=p(4)/2;
cb.Position=p;
set(gca, 'OuterPosition', [0 p(2)+2*p(4) 1 1-p(2)-2*p(4)]);
```

```

35  % hide the element edge lines
    if isfield(img, 'elems') && (length(img.elems(:,1)) < 500)
        set(hh, 'EdgeColor', [0.9 0.9 0.9]);
    else
        set(hh, 'EdgeColor', 'none');
    end
40
    lines = [];
    opt.show_surface = 1;
    if opt.show_surface && size(img.fwd_model.nodes,2) == 2 % 2d
        % draw the surface
45     bb = find_boundary(img.fwd_model.elems);
        nn = img.fwd_model.nodes;
        % find the normals, drop any that are more than 45 degrees off of vertical
        n = (nn(bb(:,1),:) - nn(bb(:,2),:)) * [0 1; 1 0]; % for 2D
        n = n ./ repmat(abs(n*[1 j]'),1,2);
50     for i = find((abs(n(:,2)) > sind(60)) & ...
                (nn(bb(:,1),2) > max(nn(:,2))/2 + min(nn(:,2))/2))'
            bbi = bb(i,:);
            h = line(nn(bbi,1),nn(bbi,2));
            set(h, 'LineWidth', 1);
55     set(h, 'Color', [0 0 0]);
            lines = [ lines h ];
        end
    end
    t = gca;
60     hh = [ hh lines t t.Children(:) ' ];

    if length(zoom) == 0
        idx = find(img.elem_data > clim(1));
        xy = interp_mesh(img.fwd_model);
65     xymin = max(xy(idx,:), [], 1); xymin = min(xy(idx,:), [], 1);
        zoom = [ xymin; xymin ];
        zoom = zoom(:);
        zoom(4) = zoom(4) + (zoom(4)-zoom(3))*0.1; % +10% above (surface)
        zoom(3) = zoom(3) - (zoom(4)-zoom(3))*0.2; % -20% below
70     end
    axis(zoom);

```

A.4 File Exchange

Listing A.7: roundsd.m

```

function y=roundsd(x,n,method)
%ROUNDSD Round with fixed significant digits
% ROUNDSD(X,N) rounds the elements of X towards the nearest number with
% N significant digits.
5 %
% ROUNDSD(X,N,METHOD) uses following methods for rounding:
% 'round' - nearest (default)
% 'floor' - towards minus infinity
% 'ceil' - towards infinity
10 % 'fix' - towards zero

```

```
%  
%  
% Examples:  
% roundsd(0.012345,3) returns 0.0123  
% roundsd(12345,2) returns 12000  
15 % roundsd(12.345,4,'ceil') returns 12.35  
%  
% See also Matlab's functions ROUND, ROUND10, FLOOR, CEIL, FIX, and  
% ROUNDN (Mapping Toolbox).  
%  
20 % Author: Francois Beauducel <beauducel@ipgp.fr>  
% Institut de Physique du Globe de Paris  
%  
% Acknowledgments: Edward Zechmann, Daniel Armyr, Yuri Kotliarov  
%  
25 % Created: 2009-01-16  
% Updated: 2015-04-03  
  
% Copyright (c) 2015, Francois Beauducel, covered by BSD License.  
% All rights reserved.  
30 %  
% Redistribution and use in source and binary forms, with or without  
% modification, are permitted provided that the following conditions are  
% met:  
%  
35 % * Redistributions of source code must retain the above copyright  
% notice, this list of conditions and the following disclaimer.  
% * Redistributions in binary form must reproduce the above copyright  
% notice, this list of conditions and the following disclaimer in  
% the documentation and/or other materials provided with the distribution  
40 %  
% THIS SOFTWARE IS PROVIDED BY THE COPYRIGHT HOLDERS AND CONTRIBUTORS "AS IS"  
% AND ANY EXPRESS OR IMPLIED WARRANTIES, INCLUDING, BUT NOT LIMITED TO, THE  
% IMPLIED WARRANTIES OF MERCHANTABILITY AND FITNESS FOR A PARTICULAR PURPOSE  
% ARE DISCLAIMED. IN NO EVENT SHALL THE COPYRIGHT OWNER OR CONTRIBUTORS BE  
45 % LIABLE FOR ANY DIRECT, INDIRECT, INCIDENTAL, SPECIAL, EXEMPLARY, OR  
% CONSEQUENTIAL DAMAGES (INCLUDING, BUT NOT LIMITED TO, PROCUREMENT OF  
% SUBSTITUTE GOODS OR SERVICES; LOSS OF USE, DATA, OR PROFITS; OR BUSINESS  
% INTERRUPTION) HOWEVER CAUSED AND ON ANY THEORY OF LIABILITY, WHETHER IN  
% CONTRACT, STRICT LIABILITY, OR TORT (INCLUDING NEGLIGENCE OR OTHERWISE)  
50 % ARISING IN ANY WAY OUT OF THE USE OF THIS SOFTWARE, EVEN IF ADVISED OF THE  
% POSSIBILITY OF SUCH DAMAGE.  
  
if nargin < 2  
    error('Not enough input arguments.')55 end  
  
if nargin > 3  
    error('Too many input arguments.')end  
60  
if ~isnumeric(x)  
    error('X argument must be numeric.')end  
65  
if ~isnumeric(n) || ~isscalar(n) || n < 0 || mod(n,1) ~= 0  
    error('N argument must be a scalar positive integer.')end
```

```
end
opt = {'round','floor','ceil','fix'};
70
if nargin < 3
    method = opt{1};
else
    if ~ischar(method) || ~ismember(opt,method)
75        error('METHOD argument is invalid.')
    end
end

% — the generic formula was:
80 %og = 10.^(floor(log10(abs(x)) - n + 1));
%y = feval(method,x./og).*og;

% — but to avoid numerical noise, we must treat separately positive and
% negative exponents, because:
85 % 3.55/0.1 - 35.5 is -7.105427357601e-15
% 3.55*10 - 35.5 is 0
e = floor(log10(abs(x)) - n + 1);
og = 10.^abs(e);
y = feval(method,x./og).*og;
90 k = find(e<0);
if ~isempty(k)
    y(k) = feval(method,x(k).*og(k))./og(k);
end
y(x==0) = 0;
```